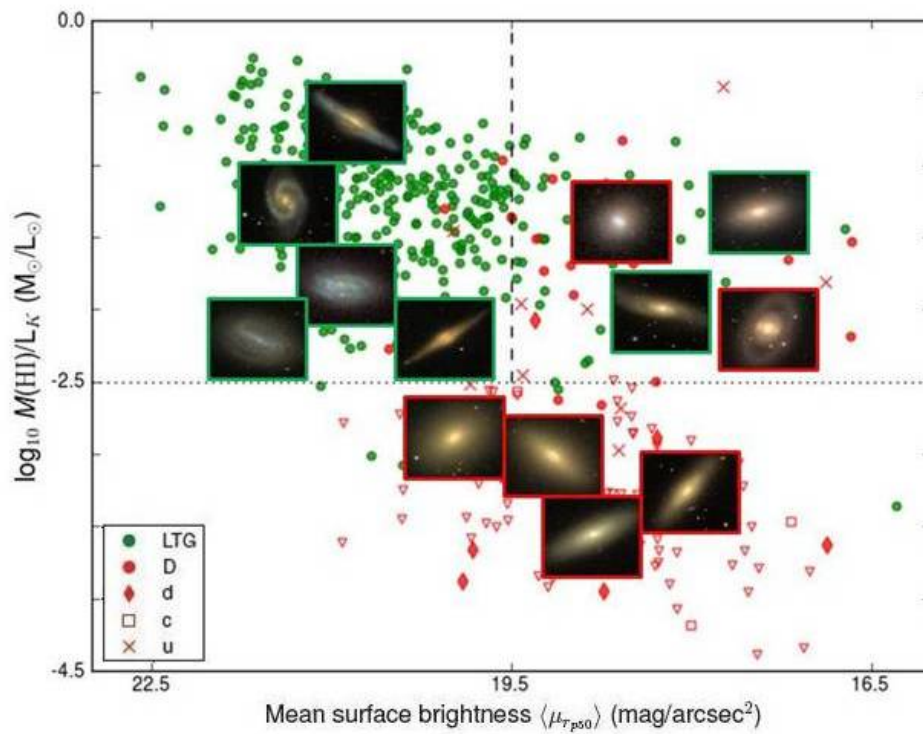


Galaxy morphology in the era of large surveys: impact on HI studies



HI mass-to-luminosity ratio against mean surface brightness. SDSS postage stamps have been placed for several galaxies, with red or green border to indicate early- or late-type, respectively.

NANCY IRISARRI
SUPERVISED BY PAOLO SERRA AND TOM OOSTERLOO
Kapteyn Astronomical Institute
University of Groningen

August 22, 2012

ABSTRACT

Currently available large-scale surveys at optical wavelengths have allowed the study of galaxy formation and evolution with samples up to hundreds of thousands of galaxies. Galaxies are typically selected by visual inspection of their optical morphology or by automated classification methods. In the near future we will study samples of thousands of objects for which visual inspection is virtually impossible. One example are upcoming next-generation neutral hydrogen (HI) surveys that will greatly expand the number of high-resolution observations of this key component. In this thesis we first compare visual classifications of galaxies to automated classification methods that use galaxy concentration and mean surface brightness. We then analyze the impact of the different selection procedures on the result of HI studies.

CONTENTS

1	PROJECT GOALS	1
1.1	Introduction	1
1.2	Galaxy classification methods	3
1.3	ATLAS ^{3D} sample	5
1.4	Outline of the thesis	6
2	THE SAMPLE	7
2.1	SDSS (DR8) query	7
2.2	Refinement of SDSS cross-identification	8
2.3	Visual inspection of multiple matches	9
2.4	Visual inspection of distant matches	9
2.5	Magnitude-vs-radius outliers	9
2.6	NYU-VAGC cross-identification	10
2.7	Final sample	11
3	PHOTOMETRIC PROPERTIES	15
3.1	Concentration index	15
3.2	Mean surface brightness	22
3.3	Axis ratio	23
3.4	Profile type	26
3.5	Sérsic index	28
3.6	Summary	28
4	HI PROPERTIES	31
4.1	HI mass	32
4.2	HI mass-to-luminosity ratio	34
4.3	Galaxies classified by automated methods	38
5	SUMMARY	40
6	APPENDIX OF TABLES	42
6.1	Galaxies selected from multiple matches	42
6.2	Galaxies with distance > 5 arcsec	43
6.3	Magnitude-vs-radius outliers	44
	BIBLIOGRAPHY	45

PROJECT GOALS

1.1 INTRODUCTION

Large-scale surveys at optical wavelengths have provided images and spectra for thousands of galaxies in the nearby Universe. Especially the Sloan Digital Sky Survey (SDSS, [York et al. 2000](#)), with its dedicated 2.5-meter telescope now in operation for more than ten years and its digital data products, is an immense supply of information. Astronomical research has exploited this supply, yielding important insights into the formation and evolution of galaxies out to moderate redshift.

For example, based on samples including up to hundreds of thousands of SDSS galaxies, it has been possible to study on a strong statistical basis: the relation between galaxy global color and morphology (e. g., [Strateva et al. 2001](#)); the variation of star-formation rate as a function of environment density (e. g., [Gómez et al. 2003](#); [Balogh et al. 2004](#)); the luminosity function of galaxies and its dependence on galaxy morphology (e. g., [Nakamura et al. 2003](#)); the star formation history of galaxies as a function of stellar mass (e. g., [Kauffmann et al. 2003](#)); the distribution of galaxy sizes (e. g., [Shen et al. 2003](#)); the relation between galaxies' black-hole and bulge (e. g., [Heckman et al. 2004](#)); the relation between galaxy mass and metallicity (e. g., [Tremonti et al. 2004](#)); and the way galaxy color and luminosity change as a function of environment density (e. g., [Blanton et al. 2005b](#)).

Furthermore, SDSS data have been successfully combined with data at other wavelengths. A good example is [Bell et al. \(2003\)](#) who combined large galaxy samples from the SDSS and the Two Micron All Sky Survey (2MASS, [Skrutskie et al. 2006](#)). Taking advantage of the fact that 2MASS provides a view of galaxies' stellar component essentially unaffected by dust, they were able to determine both the luminosity and stellar mass functions of the galaxy population. However galaxies are not made of just stars and available surveys like SDSS or 2MASS give no information about other fundamental components of galaxies.

An important example is galaxies' neutral hydrogen (HI) gas. This (and cold gas in general) is important because it is the material from which new stars form. Also, cold gas can dissipate energy and typically settles on an approximately flat disc, the place where new stars are then formed. Therefore, HI is an important driver of both galaxies' stellar content and morphology and its observation is a fundamental complement to surveys like SDSS or 2MASS.

Currently, HI observations are available mainly for galaxies in the local Universe. Moreover, the vast majority of them has been taken at low angular resolution with single-dish telescopes. Examples of single-dish surveys are the HI Parkes All-Sky Sur-

vey (HIPASS, Barnes et al. 2001; Meyer et al. 2004; Wong et al. 2006) and the Arecibo Legacy Fast ALFA (ALFALFA, Giovanelli et al. 2005) survey which cover large areas of the sky (in the case of HIPASS the whole sky between $\delta = -90$ deg and $\delta = +30$ deg, for a total of $\sim 30,000$ deg², while ALFALFA covers 7000 deg²). These surveys reach $z \sim 0.05$ and have an angular resolution of 15 and 3 arcmin, respectively.

However, the study of many physical processes that influence galaxy formation and evolution (e. g., dynamical interactions, gas accretion, tidal or ram-pressure gas stripping in dense environments) require high-resolution H I observations. For example, Very Large Array observations of spiral galaxies inside the Virgo galaxy cluster revealed a strong variation of H I morphology as a function of location within the cluster, and a strong difference compared to field spirals (Chung et al. 2009). Another example is the observation of H I in early-type galaxies which reveals that these galaxies contain H I too, and their H I morphology varies strongly with environment density (Morganti et al. 2006; Oosterloo et al. 2010b; Serra et al. 2012). The lack of high-resolution H I imaging for samples comparable to those observed in optical surveys is a major limitation for research in galaxy formation and evolution.

This situation will soon be improved by the next-generation H I surveys. A focal plane array system called Apertif has been developed for use with the Westerbork Synthesis Radio Telescope (WSRT, Verheijen et al. 2008). Apertif increases the instantaneous field of view of the WSRT to 8 deg² (a factor of 25 larger than the current field of view) such that high-resolution observations of large and deep volumes of the Universe can be carried out (Oosterloo et al. 2010a). Also, the Australian SKA Pathfinder (ASKAP) is under construction and will consist of 36 antennas equipped with phased array feeds for a field of view of approximately 30 deg² (Meyer 2009). These instruments together will observe H I in galaxies in the northern and southern hemispheres out to redshift $z \sim 0.2$ and can achieve an angular resolution of 10 to 30 arcsec.

Thanks to the surveys mentioned above, in the near future it will be possible to complement fully optical catalogs such as the SDSS with information about the H I content of galaxies. As we have argued, this will represent a major step forward for research on galaxy evolution. It will also be a major change in the way we study the *resolved* H I properties of galaxies. So far we have had to deal with samples of, at most, some tens of galaxies. Typically these were selected upon visual inspection of their optical morphology, for example early-type vs. spiral galaxies (van der Hulst 2002; Chung et al. 2009; Serra et al. 2012). In the near future we will study samples of thousands of objects for which such selection is virtually impossible. Instead, we will have to select galaxies based on parameters which are measured as part of the data reduction and analysis pipeline. What parameters should we use for a given science question? In particular, will it still be possible to study (and contrast the properties of) samples of early-type and spiral galaxies? If not, what are the differences in sample selection? This is an important point to be able to compare future results to previous ones.

The questions posed above boil down to the question we seek to answer with this project. How does galaxy automated classification map onto visual, morphological classification? And having answered that question, what is the impact of the different selection procedures on the result of H I studies? In the rest of this chapter we discuss some aspects of galaxy morphology which are relevant for our work (§1.2). We then

introduce the ATLAS^{3D} sample of nearby galaxies, which is the basis of our analysis (§1.3). Finally, we give a brief outline of the thesis (§1.4).

1.2 GALAXY CLASSIFICATION METHODS

Galaxies' morphological classification has a long history. It began almost 100 years ago, soon after they were recognized as objects outside of our Milky Way. As is well known, Edwin Hubble devised the influential tuning fork diagram to categorize galaxies based only on their visual structure. In the seminal investigation of 400 extragalactic objects that details the formulation of his diagram, Hubble (1926) writes about the descriptive nature of the classification and its deliberate independence from any theory. However, in theoretical studies of rotating and gravitating gaseous masses the contemporary Jeans (1920) found an evolutionary path for the models that was almost identical to the observational results of Hubble. Even at this early point of what we now know is a rich and intricate field evidence was found about the possible connection between the shape and physics of galaxies.

In Hubble's classification scheme galaxies are divided into two main families: ellipticals and spirals, with lenticulars as an intermediate class. Ellipticals and lenticulars are commonly referred to as early-type galaxies (ETGs), while spirals are also called late-type galaxies (LTGs). ETGs contain mostly old red stars, but some show evidence of recent star formation. These galaxies are preferentially found in rich clusters of galaxies, and the largest of them are found in the densest parts of clusters. Though all ETGs appear to be roughly roundish, it has been shown that structural differences exist between large, bright ETGs and small, faint ones. For example, the ATLAS^{3D} project has successfully identified two distinct morphologies in ETGs, such that they can be separated into fast rotators and slow rotators (Cappellari et al. 2011a). Visually ETGs have almost no features such as spiral arms or dust lanes while stellar discs are quite frequent.

The surface brightness distribution of large ETGs is usually fitted best by an $r^{1/4}$ law (de Vaucouleurs 1948):

$$\mu(r) = \mu_e + 8.3268 \left[\left(\frac{r}{r_e} \right)^{1/4} - 1 \right] \quad (1)$$

where r_e is the projected half-light radius and μ_e is the surface brightness level at r_e . In some cases a better fit to the surface brightness distribution is obtained with the Sérsic profile (Sérsic 1963):

$$\mu(r) = \mu_e + \frac{2.5b_n}{\ln 10} \left[\left(\frac{r}{r_e} \right)^{1/n} - 1 \right] \quad (2)$$

where n is the Sérsic index which together with the constant b_n describes the shape of the profile. The index n can serve to discriminate between bulge-dominated ($n=4$) and disc-dominated ($n=1$) galaxies. An image of an ATLAS^{3D} ETG is shown in Figure 1.

The other kind of galaxies included in Hubble's scheme are spiral galaxies (or LTGs). This type of galaxy is named after the structures seen in the optical bands as bright spiral arms, where hot young stars and most of the gas out of which they form are

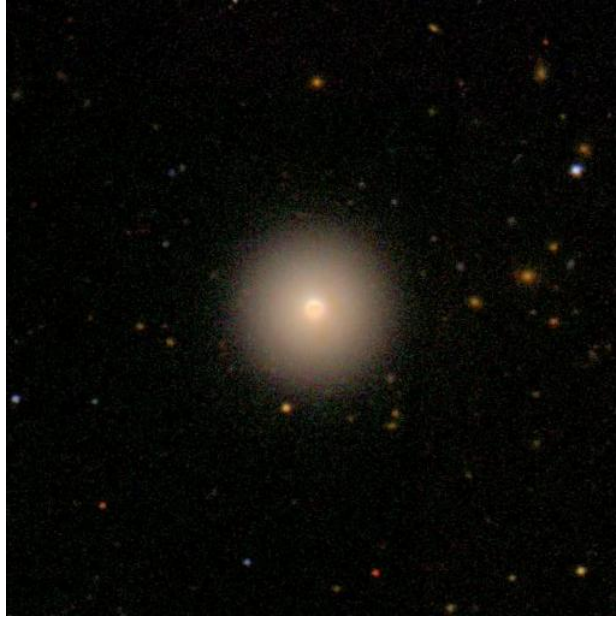


Figure 1: NGC 3457 as example of an ATLAS^{3D} early-type galaxy (ETG). *Credit: SDSS (DR8).*

found. LTGs have a central bulge and a disk, with a range of variations in the bulge-to-disc (B/D) ratios.

Theoretically the surface brightness profiles of LTGs can be fitted best by separation into two components: one for the bulge and one for the disk. The profile of the bulge can be treated similarly to ellipticals as it typically follows a light profile which can be parameterised with a Sérsic index $n > 1$. Meanwhile the disk is frequently fitted with an exponential profile:

$$\mu(r) = \mu_0 + 1.09\left(\frac{r}{h_r}\right) \quad (3)$$

where h_r is the characteristic scale length of a disk along its mid-plane and μ_0 is the surface brightness at the center. The SDSS fits a de Vaucouleurs and an exponential model to the profiles of galaxies. An image of an ATLAS^{3D} LTG is shown in [Figure 2](#).

The classification of galaxies into ETGs and LTGs (and sub-groups within these two families) is traditionally done either by visual inspection of images or by employing automated classification methods. Visual inspection by a trained observer has proven to be the most accurate method, while also providing consistent classifications. However, this method can be very time-consuming when one considers the large amounts of galaxies observed in surveys like the SDSS.

Automated classification is traditionally based on cuts in a single photometric parameter (e.g., galaxy concentration, color) or a combination of parameters, such as color-magnitude diagrams which give clues about important differences in galaxy populations. This methodology is by nature much quicker and should in principle give similar results. For example, if spiral galaxies are discs and ETGs have higher Sérsic index, it should be possible to separate these two families based on the light concentration (the concentration of an ideal Sérsic profile increases with n). However,



Figure 2: NGC 2710 as example of an ATLAS^{3D} LTG galaxy. Credit: SDSS (DR8).

real galaxies are complex systems and the use of simple parameters provides just a crude classification, which can be less accurate than visual ones and may not be appropriate to understand the fine details of galaxy evolution.

In the present work, we start from a sample of visually classified galaxies (the ATLAS^{3D} sample) and analyze how the SDSS photometric parameters of galaxies in the sample map onto the visual morphologies. Since these galaxies have also been observed in H I we can compare the result of studying H I properties as a function of visual morphology to that of studying H I properties as a function of SDSS parameters.

1.3 ATLAS^{3D} SAMPLE

The sample studied in this work is extracted from the ATLAS^{3D} parent sample, which is described in Cappellari et al. (2011a). The sample is volume limited, with a maximum galaxy distance of 42 Mpc. Within the sample volume only galaxies brighter than 2MASS absolute total magnitude $M_K = -21.5$ mag are selected (corresponding to SDSS r -band absolute magnitude $M_r \lesssim -18.9$ mag). The near-infrared magnitude limit allows selection of galaxies with a similar stellar mass, irrespective of their dust content. The luminosity function shows that the sample is representative of galaxies in the nearby Universe as it agrees with the luminosity function of a much larger sample (Figure 3 in Cappellari et al. 2011a).

Galaxies in the ATLAS^{3D} parent sample were classified based on visual inspection of optical images. Following the classical definitions, a galaxy is classified as an early-type (ETG) if it has no spiral arms or a large dust lane when seen edge-on. Other galaxies are classified as spirals or late-type (LTGs). The sample is classified using visual morphology as opposed to, e.g. color, for robustness against dust content and galaxy inclination. Color images from the SDSS DR7 (Abazajian et al. 2009) were avail-

able and used for 82% of the parent sample, while the remaining objects were classified using *B*-band DSS2-blue images in the Online Digitized Sky Survey¹. From the parent sample of 871 galaxies, Cappellari et al. (2011a) classifies 260 as ETGs which make up the ATLAS^{3D} main sample, and the remaining 611 classified as spirals we refer to here as LTGs.

In addition, the ATLAS^{3D} main sample of ETGs is probed for H I (Serra et al. 2012). The ATLAS^{3D} H I survey contains H I information for 166 ETGs, which we also discuss. The combination of the use of visual morphology for galaxy classification, the availability of most of the galaxies in the SDSS, and the H I data make the ATLAS^{3D} parent sample an adequate choice for studying our project goals.

1.4 OUTLINE OF THE THESIS

We first look for ATLAS^{3D} parent sample galaxies in the SDSS (DR8) and find photometric parameters for most of these (§2). Then we compare the photometric properties of the ATLAS^{3D} ETGs and LTGs by using several SDSS parameters often used in automated morphological classifications (§3). Finally, we analyze the H I properties of galaxies as a function of SDSS parameters and visual morphology (§4). We close with a summary of the most important results (§5).

¹ <http://archive.eso.org/dss>

THE SAMPLE

In this chapter we discuss the sample selection, which consists of galaxies in the ATLAS^{3D} parent sample that we could find in the SDSS catalog. For each of the galaxies the SDSS provides key photometric measurements that can be used to study the differences between ETGs and LTGs. As is discussed below, we first attempt to find a match for each ATLAS^{3D} galaxy in the SDSS catalog.

In §2.1 we describe the SDSS (DR8) query and in §2.2 a Python script needed to refine the matching. After the query and script we have multiple matches, distant matches, and magnitude-vs-size outliers which we discriminate further in §2.3, §2.4, and §2.5, respectively.

2.1 SDSS (DR8) QUERY

The SDSS CrossID for DR8 webpage¹ provides the facility of uploading a file with a user-defined list of object positions. We used two text tables, one for ETGs and one for LTGs, that contain the right ascension and declination of the galaxies (Tables 3 and 4² in Cappellari et al. 2011a). On the webpage we made the following selections:

- *Search type*: Images (PhotoObj).
- *Search scope*: All Nearby Primary Objects.
- *Upload type*: RA, dec.
- *Search radius [arcmin] (Max 3.0 arcmin)*: 1.0 arcmin.

In addition, we modified the SQL query box to retrieve only objects classified as galaxies.

We found cross-identifications for most of the ATLAS^{3D} parent sample, but some galaxies had multiple or no matches. Therefore it was necessary to refine some of the matches and select if possible a single SDSS object for each galaxy, as will be explained in the following sections.

¹ Found at <http://skyserver.sdss3.org/dr8/en/tools/crossid/crossid.asp>.

² Published in full at <http://purl.org/atlas3d>.

2.2 REFINEMENT OF SDSS CROSS-IDENTIFICATION

We used a Python code to attempt to select a single cross-identification from the output described in the section above. The code calculates the distance between the ATLAS^{3D} galaxy and its matches using the following formula:

$$\text{distance} = \arccos[\sin(\alpha_1) * \sin(\alpha_2) + \cos(\alpha_1) * \cos(\alpha_2) * \cos(\delta_1 - \delta_2)] \quad (4)$$

where

- α_1 ATLAS^{3D} right ascension,
- δ_1 ATLAS^{3D} declination,
- α_2 SDSS right ascension,
- δ_2 SDSS declination.

Ideally the best match to each galaxy is a single SDSS object with minimum distance in the above formula. However, it is expected that there are several SDSS objects close to the ATLAS^{3D} galaxy. We therefore consider as potentially good matches all SDSS objects with a distance less than 10% and/or which are closer than 10 arcsec to the distance of the nearest SDSS object. Also, in the code we set a limit of SDSS magnitude $r < 17$ according to the ATLAS^{3D} selection (§1.3), and since SDSS galaxies have $r-K < 5$ (Obrić et al. 2006). Adding these criteria to the cross-identification, we obtain no match for 38 ETGs and 84 LTGs, a single match for 220 ETGs and 502 LTGs, and multiple matches for 2 ETGs and 25 LTGs. We study further the latter in §2.3.

Figure 3 shows a histogram of the minimum distance using Equation 4 for each ATLAS^{3D} ETG or LTG with a single SDSS match, where both distributions are normalized by the number of galaxies it represents. As can be seen, the matching is excellent for most galaxies. However, there are 22 galaxies (2 ETGs and 20 LTGs) for which the distance is greater than 5 arcsec. We dub these cases as distant matches and study them individually in order to include or exclude the SDSS galaxy in our sample (§2.4).

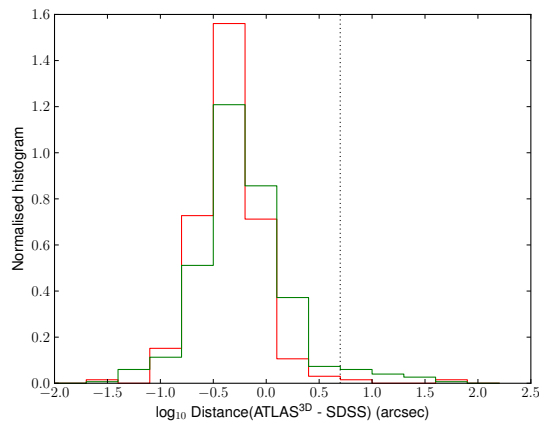


Figure 3: Normalized histogram of distance between ATLAS^{3D} ETGs (red lines) and LTGs (green lines) and corresponding SDSS cross-identified object. The 22 galaxies with distance greater than 5 arcsec (dotted line) are discussed in §2.4.

2.3 VISUAL INSPECTION OF MULTIPLE MATCHES

Our 27 galaxies with multiple matches had 2 or 3 matches. The basic procedure followed for each case was essentially the same. We consider the SDSS r -Band model magnitude, in which several cases had unreliable magnitude. Also, we make the requirement that the 90% Petrosian radius from SDSS must be larger than the effective radius given in Tables 3 and 4 of Cappellari et al. (2011a). Next, for each galaxy we query the SDSS Image List Tool³ with the right ascension and declination of all its matches. In several occasions the match was located significantly off the center of the galaxy seen in the image, which automatically discarded the SDSS object as a match. In most cases this process gave a clear choice of an SDSS match.

Appendix 6.1 shows the 20 selected galaxies and the parameters which, along with the SDSS images, were used in this process.

2.4 VISUAL INSPECTION OF DISTANT MATCHES

This section discusses the process followed to decide if we include or exclude each of the 22 galaxies with a distance between ATLAS^{3D} and SDSS coordinates greater than 5 arcsec, shown as the vertical line in the log-histogram of distances of Figure 3. We used the same criteria as for the multiple matches discussed in §2.3, namely, the model magnitude in r -Band, SDSS 90% Petrosian radius and the effective radius given in Table 3 and 4 of Cappellari et al. (2011a), and inspection of the images. For these matches, the images were a good way to decide if the SDSS cross-identification was correct. After the selection process we included in our sample 12 out of the 22 matches.

Appendix 6.2 shows the 22 galaxies and the parameters which, along with the SDSS images, were used in the discrimination. The last column indicates if it was included (I) or excluded (E) in our sample.

2.5 MAGNITUDE-VS-RADIUS OUTLIERS

We plot r -Band model magnitudes against half-light radius for the single matches described in §2.2 in Figure 4. There are 8 outliers in the plot, all of them spiral galaxies. In Appendix 6.3 we list them and provide SDSS parameters.

These LTGs all have 90% Petrosian radius much smaller than the effective radius given in Table 4 of Cappellari et al. (2011a). We inspected the images of each of the objects and found that all of them have a large bright center, patchy surface, and 4 seem to be interacting with a companion galaxy. SDSS pipeline errors could explain their position in Figure 4 and due to this we decided to exclude all of them from our sample.

We note already here that ETGs and LTGs are fairly well separated on this plane owing to their different typical light concentration. This will be one of the main points discussed in §3.

³ Found at <http://skyserver.sdss3.org/dr8/en/tools/chart/list.asp>.

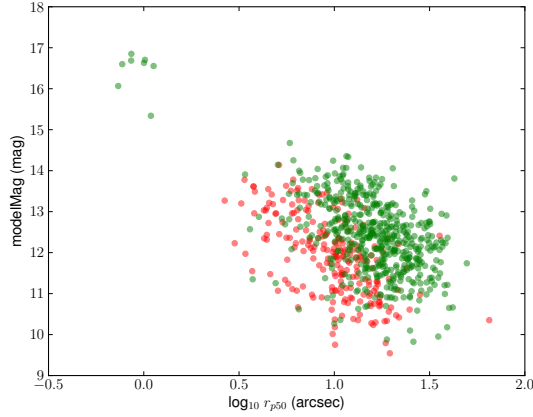


Figure 4: Model magnitude in the r -Band against \log_{10} Petrosian half-light radius for the cross-identifications of the ETGs (red circles) and LTGs (green circles).

2.6 NYU-VAGC CROSS-IDENTIFICATION

In addition to the SDSS database we make use of the New York University Value-Added Galaxy Catalog (NYU-VAGC, [Blanton et al. 2005a](#)), which is a collection of galaxies cross-matched to several catalogs, amongst them the SDSS up to its DR7. The included SDSS quantities differ from those in the SDSS Archive Servers due to a number of improvements described in [Blanton et al. \(2005a\)](#). Also, the NYU-VAGC provides a number of parameters from one-component Sérsic fits ([Blanton et al. 2005b](#)) and we analyze the Sérsic index in §3.5. For the matches described above, we search the NYU-VAGC to obtain the galaxy with minimum distance using [Equation 4](#). [Figure 5](#) shows the distribution of minimum distances for the matches found in the NYU-VAGC. Since the minimum distance is calculated between SDSS coordinates, we consider as ATLAS^{3D} matches only those galaxies with a distance < 1 arcsec in the NYU-VAGC.

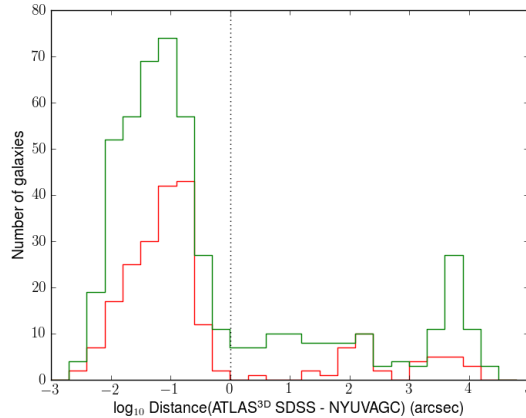


Figure 5: Histogram of distance between ATLAS^{3D} ETGs (red lines) and LTGs (green lines) and corresponding NYU-VAGC match.

This method finds 181 ETGs and 373 LTGs, while it excludes 40 ETGs and 130 LTGs. The large number of missing galaxies is possibly due to the NYU-VAGC selection criteria.

2.7 FINAL SAMPLE

In [Figure 6](#) and [Figure 7](#) we show histograms of the distribution in absolute total magnitude M_K for all 260 ETGs and 611 LTGs in the in ATLAS^{3D} parent sample, and for the final 221 ETGs and 503 LTGs selected as described above. The histograms exhibit excellent agreement in the M_K range covered, demonstrating the representativeness of our selection of 83% of the ATLAS^{3D} parent sample.

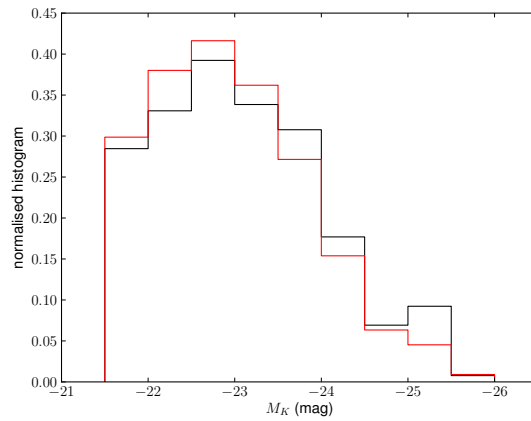


Figure 6: Normalized histogram of absolute total magnitude M_K for ATLAS^{3D} ETGs (black lines) and for those we include in our sample (red lines). Magnitudes are found in Table 3 of [Cappellari et al. \(2011a\)](#).

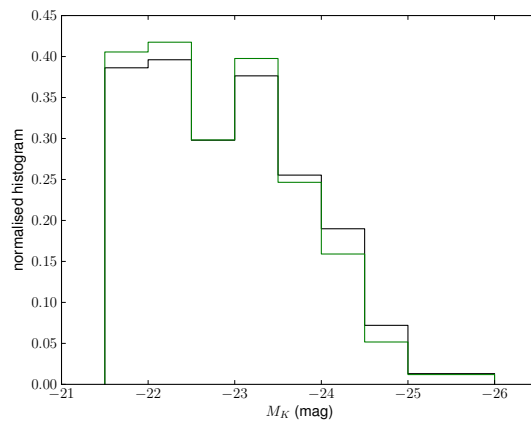


Figure 7: Normalized histogram of absolute total magnitude M_K for ATLAS^{3D} LTGs (black lines) and for those we include in our sample (green lines). Magnitudes are found in Table 4 of [Cappellari et al. \(2011a\)](#).

The Galactic extinction-corrected $g-r$ color-magnitude diagram for our sample is shown in [Figure 8](#), for a region that excludes 10 outlying galaxies (one is an ETG). The ETGs show little scatter and redder colors, and some ETGs stray into the blue cloud. LTGs, on the other hand, show no tight color-magnitude relation and are seen dispersed throughout the diagram. We have verified that this diagram is in agreement with the one derived by other members of the ATLAS^{3D} team independently using the SDSS database. The absolute magnitude M_r is calculated using

$$M_r = \text{modelMag}_r - 5 * \log(D) + 5 \quad (5)$$

where D is the distance found in Tables 3 and 4 in [Cappellari et al. \(2011a\)](#).

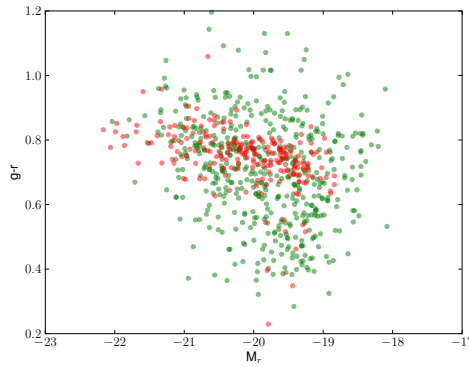


Figure 8: Galactic extinction-corrected color-magnitude diagram for our sample of ETGs (red circles) and LTGs (green circles). Magnitudes are found in Tables 3 and 4 of [Cappellari et al. \(2011a\)](#).

The method of background subtraction used by the SDSS *photo* pipeline underestimates the flux, size, and concentration of large galaxies ([Blanton et al. 2005b](#); [Hyde & Bernardi 2009](#); [West et al. 2010](#)). However, as shown in [Figure 9](#) the galaxies in our sample have Petrosian diameters of less than a few arcminutes.

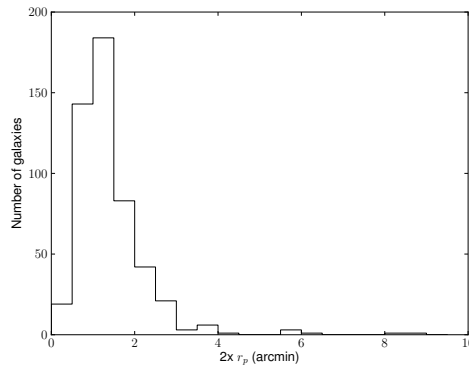


Figure 9: Histogram of Petrosian radii extracted from the SDSS for our selection of ATLAS^{3D} ETGs and LTGs.

[Figure 10](#) and [Figure 11](#) show the sky distribution of the ATLAS^{3D} parent sample along with the matches selected as described in this chapter.

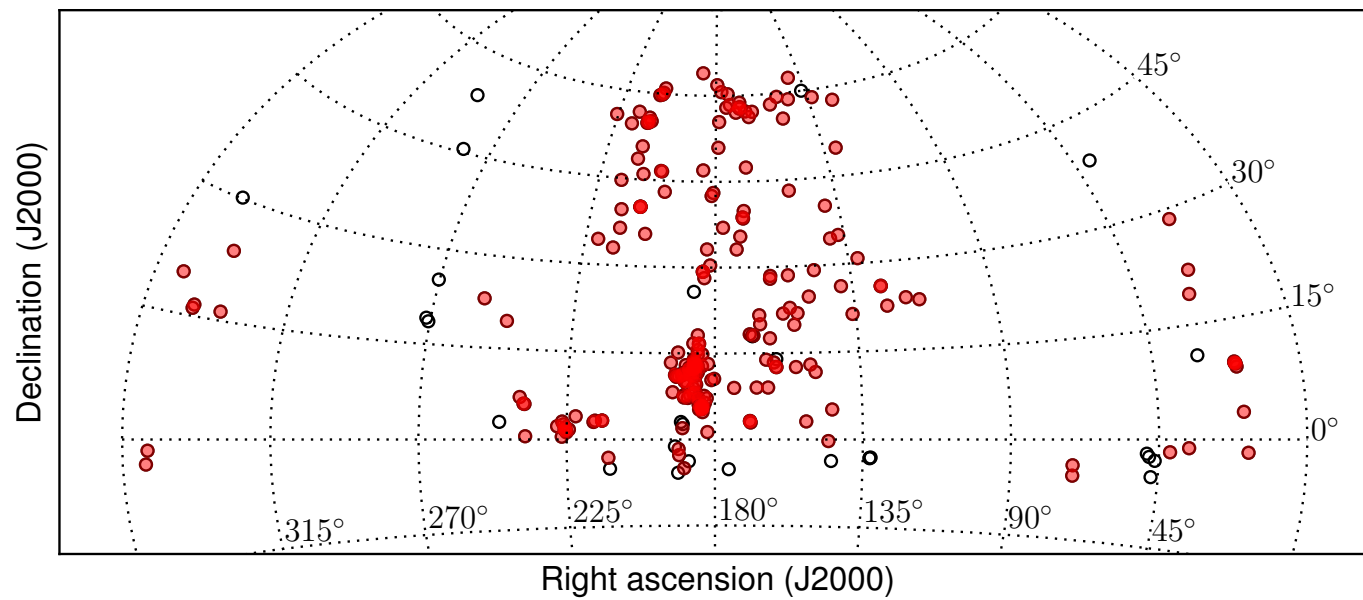


Figure 10: Sky distribution of ATLAS^{3D} ETGs (open black circles) and the 221 with SDSS counterparts we include (red circles). Right ascension and declination are given in Table 3 of [Cappellari et al. \(2011a\)](#).

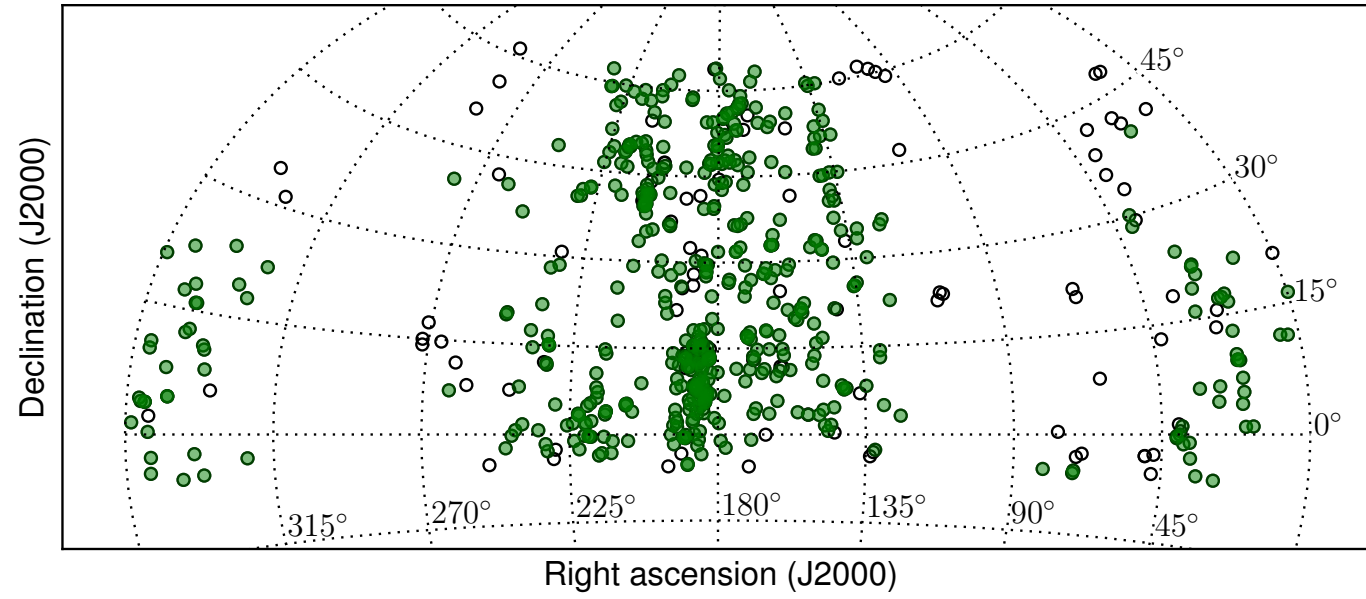


Figure 11: Sky distribution of ATLAS^{3D} LTGs (open black circles) and the 503 with SDSS counterparts we include (green circles). Right ascension and declination are given in Table 4 of [Cappellari et al. \(2011a\)](#).

3

PHOTOMETRIC PROPERTIES OF VISUALLY CLASSIFIED EARLY-TYPE AND SPIRAL GALAXIES

In this chapter we analyze the photometric properties of galaxies in the ATLAS^{3D} sample and study how these properties map onto the visual classification into the ETG and LTG families. Namely, we analyze the concentration index (§3.1), mean surface brightness (§3.2), axis ratio (§3.3), light profile type (§3.4) and Sérsic index (§3.5). Widely-used galaxy classification schemes which employ these parameters in automated methods are also discussed. In §3.6 we summarize the results.

3.1 CONCENTRATION INDEX

In this section we discuss the concentration index, a parameter reported to correlate well with the early- and late-type morphological classifications (e. g., [Shimasaku et al. 2001](#); [Strateva et al. 2001](#); [Nakamura et al. 2003](#); [Shen et al. 2003](#)).

Almost 50 years ago, [Morgan \(1958\)](#) proposed a galaxy classification system which used light concentration as its main criterion. In this scheme, which is sometimes referred to as the Yerkes system, there are two extreme types: galaxies having low light concentration, namely type *a*, and at the other end galaxies with the most extreme central concentration of light, namely type *k*. The letter designations are given since type *a* galaxies tend to have early-type (A) integrated spectra, due to a dominant young stellar population, while type *k* galaxies tend to have late-type (K) integrated spectra, dominated by old stars. Thus, unlike the Hubble classification system, this one takes into account the correspondence between galaxy morphology, manifested in the concentration property, and stellar populations. Galaxies with an intermediate degree of concentration show also intermediate-type spectra, and these are classified exclusively by the concentration criterion into the types *af*, *f*, *fg*, *g*, and *gk*. Other intricacies of morphology are included in the Yerkes system, but a description of them is outside the scope of this discussion.

[Morgan \(1958\)](#) used visual inspection of photographic plates to establish his classification system. More objective measures of concentration are now available and one used widely is the concentration index, which is defined as the ratio of the radius containing 90% of the Petrosian flux ([Petrosian 1976](#)) to the radius containing 50% of said flux, $C \equiv r_{p90}/r_{p50}$. For surface brightness distributions described purely by a de Vaucouleurs profile the concentration index is ~ 5.5 , while for a profile described by an exponential law the concentration index is lower at ~ 2.3 ([Strateva et al. 2001](#)). We then expect that bulge-dominated ETGs (and also the bulges of spiral galaxies) with de Vaucouleurs light profiles will have higher concentration indices as compared to

those of disc-dominated LTGs with exponential light profiles. The essence of the concentration index is that it can and has been used as a proxy for galaxies' bulge-to-total light (B/T) ratio (e.g., [Conselice 2003](#)).

With this in mind we analyze the concentration of our sample of ATLAS^{3D} galaxies. It is known that galaxies with Petrosian half-light radius $r_{p50} < 2''$ suffer from large seeing effects which would in turn affect the measured concentration index. As can be seen from [Figure 12](#) we can leave this caveat aside in our analysis. We derive the concentration index using the SDSS *r*-band parameters *petroR90_r* and *petroR50_r*, and show its distribution for ETGs and LTGs in the histogram of [Figure 13](#). Each distribution has been normalized by the total number of galaxies in the respective sub-sample. The histogram shows that ETGs mostly have high concentration indices, while the LTG distribution peaks at lower concentration indices. However, the two distributions overlap significantly and a large fraction of LTGs have *C* values as high as that of typical ETGs.

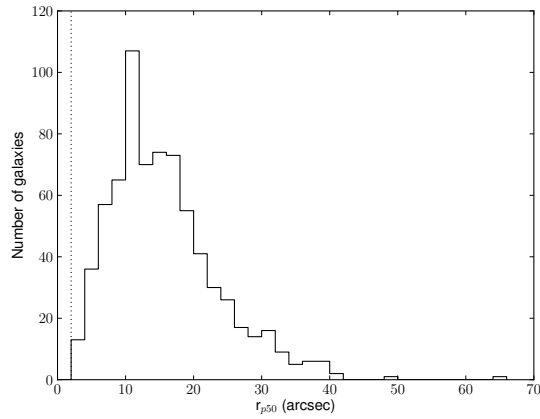


Figure 12: Petrosian half-light radius of all galaxies in our sample. Dotted line is at $r_{p50} = 2''$.

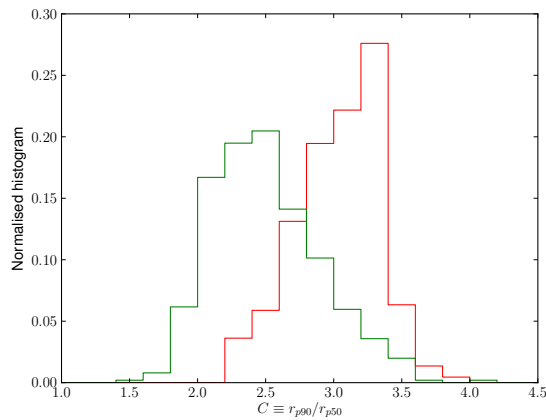


Figure 13: Normalized histogram of concentration index of ATLAS^{3D} ETGs (green lines) and LTGs (red lines) included in our study.

In order to compare automated galaxy classification based on the concentration index to visual classification we calculate the reliability and completeness of samples of ETGs and LTGs defined adopting a cut in concentration. Given the above discussion, we take galaxies with $C \geq C_0$ as the family representing ETGs and galaxies with $C < C_0$ as the family representing LTGs. We then study the result of this selection as a function of C_0 . To do so we define the reliability and completeness of this selection as follows:

$$\text{reliability}_{\text{ETG}} = \frac{N_{\text{ETG}}(C \geq C_0)}{N_{\text{ETG}}(C \geq C_0) + N_{\text{LTG}}(C \geq C_0)} \quad (6)$$

$$\text{completeness}_{\text{ETG}} = \frac{N_{\text{ETG}}(C \geq C_0)}{N_{\text{ETG}}} \quad (7)$$

$$\text{reliability}_{\text{LTG}} = \frac{N_{\text{LTG}}(C < C_0)}{N_{\text{ETG}}(C < C_0) + N_{\text{LTG}}(C < C_0)} \quad (8)$$

$$\text{completeness}_{\text{LTG}} = \frac{N_{\text{LTG}}(C < C_0)}{N_{\text{LTG}}} \quad (9)$$

where N_{ETG} and N_{LTG} are the total number of ETGs and LTGs in the sample, respectively. Given these definitions and the distributions in [Figure 13](#), we expect the completeness (reliability) of the ETG sample defined with $C \geq C_0$ to increase (decrease) with decreasing C_0 , and the completeness (reliability) of the LTG sample defined with $C < C_0$ to decrease (increase) with decreasing C_0 .

The panels of [Figure 14](#) plot the reliability (blue lines) and completeness (pink lines) for ETG sub-samples (top panel) calculated using [Equation 11](#) and [Equation 7](#), respectively, and the reliability and completeness for LTG sub-samples (bottom panel) calculated using [Equation 8](#) and [Equation 9](#), respectively. The vertical lines are the minimum and maximum concentration indices in the sub-samples. In the top panel we can see that at a concentration index $C_0 = 2.92$ the reliability and completeness of the ETGs are equal with a value of 66%, while in the bottom panel at $C_0 = 3.03$ the reliability equals the completeness of the LTGs with a value of 85%.

While one would ideally choose a concentration index that optimizes both reliability and completeness, both panels of [Figure 14](#) show a defiant interplay between these quantities. The reliability of an ETG selection based on C is never better than 72%, due to the fact that a large fraction of LTGs have concentrations as high as that of most ETGs. The optimum reliability is obtained for $C \geq 3.2$, which gives a completeness of just 36%. Meanwhile the situation is better for the LTG sub-sample such that with a cut at 2.9 we could achieve a reliability of $\sim 90\%$ and a completeness of $\sim 80\%$.

[Table 1](#) shows our results for several concentration indices adopted in the literature and discussed in this text. [Shimasaku et al. \(2001\)](#) investigate the properties of 456 bright SDSS galaxies to examine the statistical properties of color indices, scale lengths, and concentration indices as a function of morphology determined by visual inspection. Of these three parameters they include, the authors find that the concentration index is the parameter that most closely follows the visual morphology of galaxies, and can thus be used to classify them into sub-samples. Their recommendation for dichotomous classification of galaxies into early- (E and S0) and late- (Sa to Sdm and Im) types is an inverse concentration index (defined as $c \equiv r_{p50}/r_{p90}$) of 0.33. This

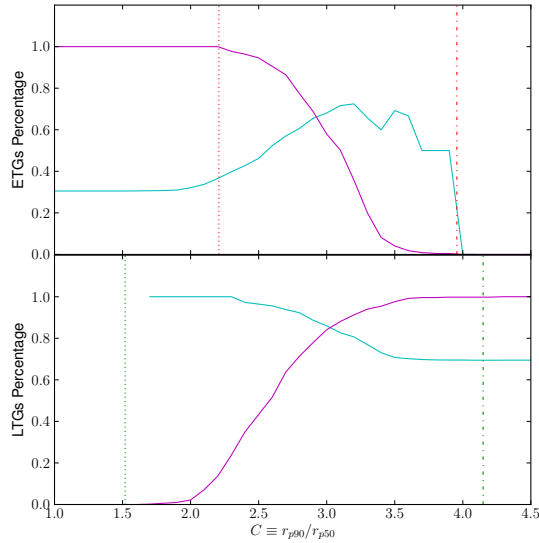


Figure 14: Reliability (light blue lines) and completeness (pink lines) as a function of concentration index for ETGs (top panel) and LTGs (bottom panel). Vertical lines are the minimum and maximum values if within the x-axis range. Empty concentration index bins and bins with few counts cause the wiggles in the lines.

corresponds to a concentration index $C \equiv r_{p90}/r_{p50}$ of 3.03. For their early-types this gives a reliability of 79% and a completeness of 68%, compared with our result of reliability 68% and completeness 55%. For their late-types it gives a reliability of 86% and completeness of 92%, compared in our LTGs with reliability of 85% and completeness of 85%. The difference in results may be explained by the different sample selections.

concentration index	ETGS		LTGS	
	rel (%)	comp (%)	rel (%)	comp (%)
2.6 (1)	52	91	94	64
2.86 (2)	63	72	89	75
2.92 (3)	66	66	87	77
3.03 (4)	68	55	85	85

Table 1: Summary of reliability (rel) and completeness (comp) achieved when applying concentration indices following (1) [Strateva et al. \(2001\)](#); (2) [Nakamura et al. \(2003\)](#); the value where reliability equals completeness (3) in the ETGs, and (4) in the LTGs (this latter value is also suggested by [Shimasaku et al. \(2001\)](#)).

In a similar study [Strateva et al. \(2001\)](#) compare the difference in reliability and completeness between classification methods using colors, spectra and morphological parameters, such as concentration. The authors inspected the spectra of 500 SDSS galaxies and the optical appearance of 287 bright SDSS galaxies to classify them into early- and late-types, and then applied concentration index cuts on these samples. Their adopted concentration index $C = 2.6$ optimizes the completeness ($\sim 73\%$ and $\sim 83\%$) and concurrently gives similar reliability ($\sim 73\%$ and $\sim 82\%$) in both samples. We apply this concentration index value as shown in [Table 1](#) and obtain a reliability of

52% and a completeness of 91% in the ETGs, while a reliability of 94% and completeness of 64% in the LTGs.

[Nair & Abraham \(2010\)](#) build a catalog of detailed visual morphological classifications of galaxies with the intention that it serves as a training set for automated classification methods. It contains $\sim 14,000$ SDSS (DR4) galaxies, which are assigned a T -type and inspected for subtle features such as bars, rings, tails, and warps. Thus both ATLAS^{3D} and this catalog contain galaxies classified using morphology from SDSS images. In contrast the latter contains ~ 19 times more galaxies, is not volume limited, and does not consider dust lanes in the visual classification process. [Figure 15](#) compares the reliability and completeness shown in [Figure 14](#) to that derived in the same manner for the [Nair & Abraham \(2010\)](#) catalog. For that sample we define as ETGs all galaxies with T -type ≤ 0.0 and as LTGs all galaxies with T -type > 0.0 . This gives 5,938 ETGs and 7,758 LTGs, while in our sample we have 221 ETGs and 503 LTGs. We take into account this difference by scaling the [Nair & Abraham \(2010\)](#) ETG reliability curve, and by scaling the ATLAS^{3D} LTG reliability curve instead in order that both LTG reliability curves are below 1.0.

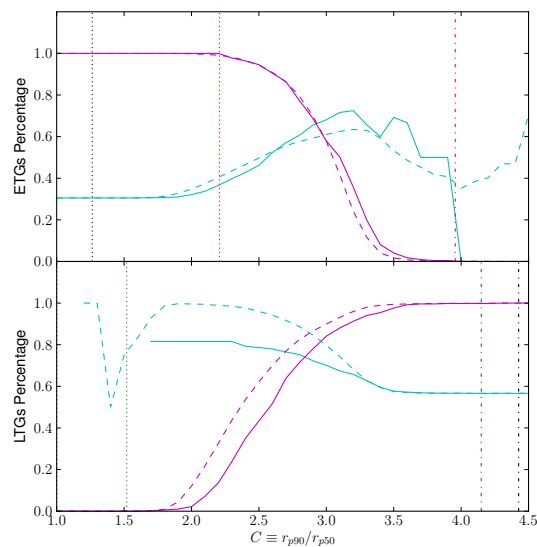


Figure 15: Comparison between reliability (light blue lines) and completeness (pink lines) as a function of concentration index for ETGs (top panel) and LTGs (bottom panel) in our sample of ATLAS^{3D} galaxies (solid lines) and [Nair & Abraham \(2010\)](#) galaxies (dashed lines). Vertical lines are the minimum and maximum values if within the x-axis range. Empty concentration index bins and bins with few counts cause the wiggles in the lines.

In both panels of [Figure 15](#) there is excellent agreement for the reliability and completeness curves between our ATLAS^{3D} sample and the [Nair & Abraham \(2010\)](#) ETG sample, and some differences for the LTG sample. This means that the same concentration index cut used to automatically determine if a galaxy is an ETG or an LTG will result in similar reliability and completeness in both the sub-samples. Therefore the classification scheme applying galaxy concentration shows very high consistency.

As was mentioned, it is expected that ETGs have higher concentration indices than LTGs. However, the distributions in Figure 13 show that ETGs and LTGs overlap significantly along the C axis. Figure 16 and Figure 17 demonstrate that this overlap exists at all galaxy luminosities. The only trend with luminosity is that bright LTGs usually avoid low C , so the overlap with the ETG family at high luminosity is even more severe (top-left panel in Figure 17).

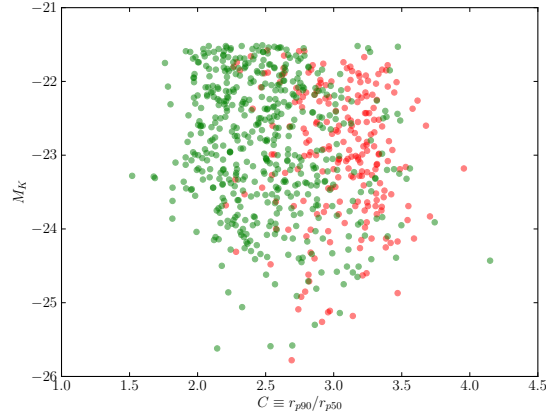


Figure 16: Absolute K-band magnitude as a function of concentration index for ETGs (green circles) and LTGs (red circles).

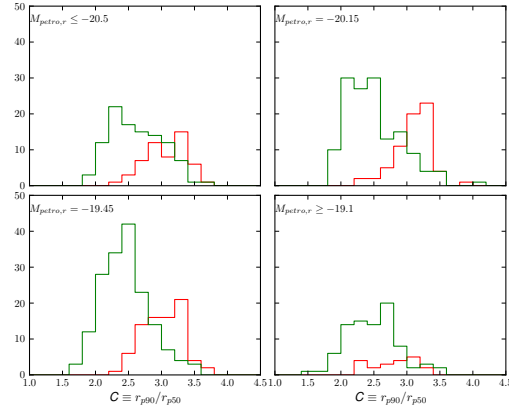


Figure 17: Histogram of concentration index of ETGs (green lines) and LTGs (red lines) in Petrosian r -band absolute magnitude bins $M_{\text{petro},r} \leq -20.5$ (top left), $-20.5 \leq M_{\text{petro},r} \leq -20.15$ (top right), $-20.15 \leq M_{\text{petro},r} \leq -19.45$ (bottom left) and $M_{\text{petro},r} \geq -19.1$ (bottom right).

Although usually concentration is believed to be a good tracer of morphology, we show here (in substantial agreement with previous results) that this is the case only at an approximate level. It is therefore natural to wonder about the optical appearance of two galaxies having similar concentration but visually classified one as an ETG and the other as a spiral. Figure 18 shows SDSS images of all ETGs and LTGs with concentration indices in the range 2.75 to 2.8. Figure 19 shows T -type histograms for galaxies in the wider concentration index range 2.7 to 3.1, showing that these LTGs

have earlier T -types than the full sample of LTGs. While visual morphologies have some similarities such as flattening and bright bulges, the outstanding difference is fine structure morphology, i. e. spiral arms, discs, and rings.

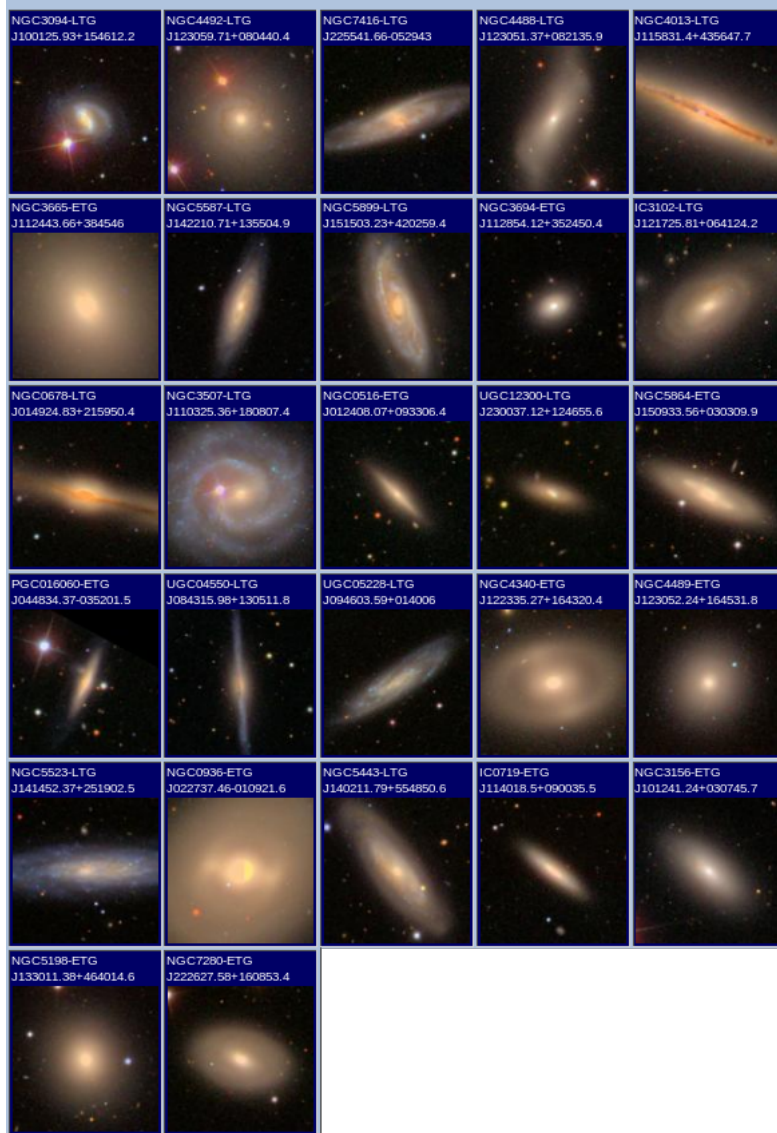


Figure 18: Compilation of all 27 galaxies, 12 ETGs and 15 LTGs, with $2.75 \leq C \leq 2.8$ on a scale of 1.6 arcsec/pix. The top row of each image shows the galaxy name and its type.

The SDSS pipeline outputs other photometric parameters that are used widely in galaxy classification and type selection. In the next sections we analyze some of these properties in an attempt to replace or refine the separation of samples into early- and late-types based on concentration.

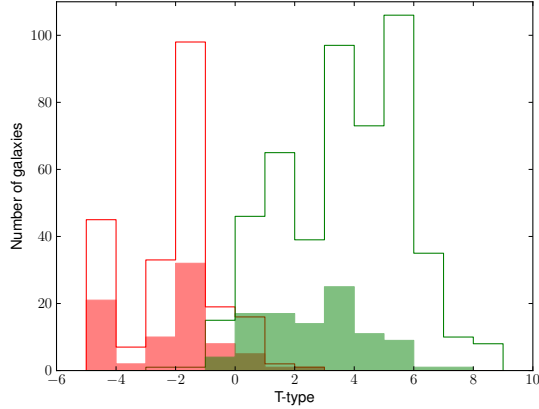


Figure 19: Histogram of T -type for ETGs (shaded red) and LTGs (shaded green) with $2.7 \leq C \leq 3.1$, and for all other ETGs (red lines) and LTGs (green lines).

3.2 MEAN SURFACE BRIGHTNESS

In this section we discuss the mean surface brightness, which similar to concentration is used as a tracer of the B/T ratio and thus correlates with visual morphology. It forms part of important scaling relations (Kormendy 1977) and linear combinations using the related quantity of stellar mass surface density and other galaxy properties (e.g., color, star formation per unit stellar mass) have been found to correlate well with cold gas fractions (Catinella et al. 2010). From the SDSS parameters $m_{\text{petro},r} = \text{petroMag}_r$ and $r_{p50} = \text{petroR50}_r$ we calculate the mean surface brightness within the Petrosian half-light radius $\langle \mu_{r_{p50}} \rangle$ using

$$\langle \mu_{r_{p50}} \rangle = m_{\text{petro},r} + 2.5 \log[2\pi(r_{p50})^2] \quad (10)$$

in which the units are $\text{mag}/\text{arcsec}^2$. The histogram for the ETGs and LTGs is shown in Figure 20, where each distribution has been normalized by the total number of galaxies in the respective sub-sample.

Concentration index correlates with mean surface brightness, as is shown in Figure 21. The figure shows that galaxies with high concentration indices have high mean surface brightnesses on an almost linear scale, though with some scatter. Thus analyses using galaxy concentration can also be made replacing it with mean surface brightness with the expectation of obtaining similar results.

Similar to our analysis of concentration-based selection, we calculate the reliability and completeness of sub-samples selected using mean surface brightness in Figure 22. Again we find that a choice must be made of a particular mean surface brightness as optimum for galaxy classification. For the ETGs reliability equals completeness at $\sim 71\%$ for $\langle \mu_{r_{p50}} \rangle \sim 19.6 \text{ mag}/\text{arcsec}^2$, and for the LTGs they are equal at $\sim 84\%$ for $\langle \mu_{r_{p50}} \rangle \sim 19.1 \text{ mag}/\text{arcsec}^2$. This result is only marginally better for the ETGs when compared to that using concentration index $C = 2.92$ which gave 66% reliability and completeness, while is essentially the same for the LTGs using $C = 3.03$ which had 85% reliability and completeness. Meanwhile, the maximum reliability that can be achieved

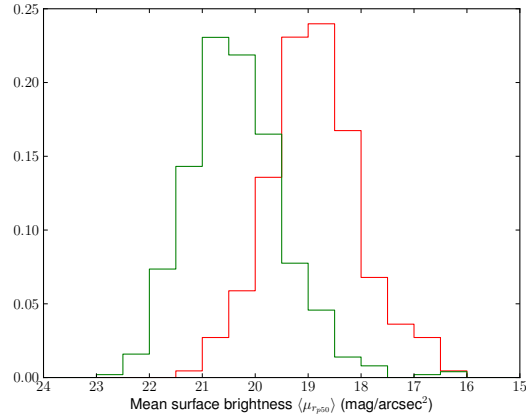


Figure 20: Normalized histogram of mean surface brightness of ETGs (green lines) and LTGs (red lines).

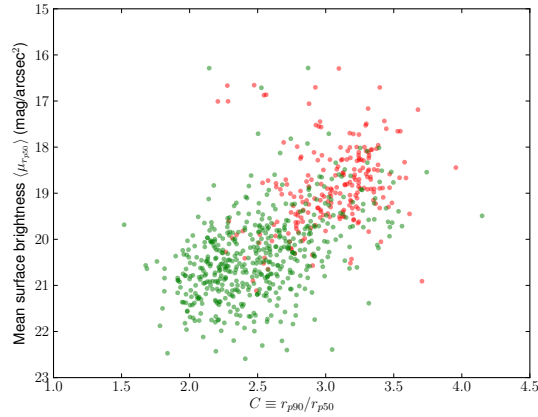


Figure 21: Mean surface brightness against concentration index for ETGs (green circles) and LTGs (red circles).

for the ETGs is $\sim 87\%$, though with a very low completeness, which is better than the maximum of 72% possible with concentration index.

3.3 AXIS RATIO

While in §3.1 we compared the amount of light in the inner parts to that in the outer parts of our galaxies, in this section we analyze the apparent flattening of the galaxies as measured by the axis ratio b/a . This parameter has been used in automated classification methods and to discriminate between early- and late-type galaxies (Sheth et al. 2003; Choi et al. 2007; Cheng et al. 2011).

Bernardi et al. (2010) analyze automated galaxy classification methods, amongst them axis ratio cuts, by applying them to two samples, one of them a large sample of galaxies classified by visual inspection in Fukugita et al. (2007). The authors find that the axis ratios of early-type galaxies are higher than the axis ratios of late-types. How-

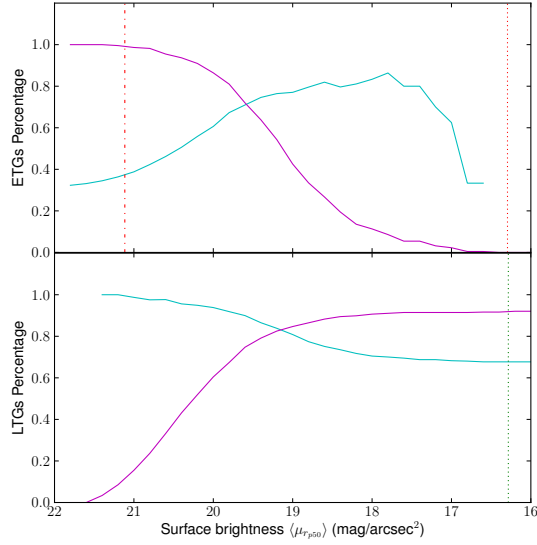


Figure 22: Reliability (light blue lines) and completeness (pink lines) as a function of mean surface brightness for ETGs (top panel) and LTGs (bottom panel). Vertical lines are the minimum and maximum values for each sub-sample if within the x-axis values. Empty bins and bins with few counts cause the wiggles in the lines.

ever, their analysis also shows that using only axis ratio cuts in automated methods produces sub-samples of galaxy types heavily contaminated by other galaxy types.

This overlap is evident in [Figure 23](#), where we analyze the axis ratio of our ATLAS^{3D} galaxies. For each of the galaxies, the SDSS pipeline fits the light profile distributions with a de Vaucouleurs and an exponential model and outputs the minor-to-major axis ratio and the likelihoods calculated from χ^2 fits to each of the models. We use the axis ratio derived from the profile with the largest likelihood.

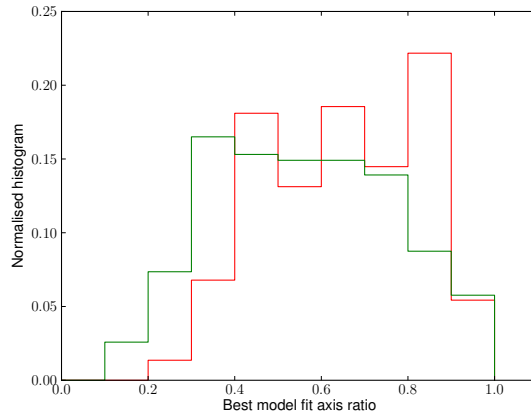


Figure 23: Normalized histogram of best fit axis ratio, where each distribution has been normalized by the total number of galaxies in the respective sub-sample.

Also, [Cheng et al. \(2011\)](#) visually classify 984 red sequence SDSS galaxies into E, S0, and Sa. They then develop an automated method that combines the bulge to light fraction (where a pure disc has $B/T = 0$), the axis ratio derived from isophotes in the SDSS pipeline, and the clumpiness and asymmetry of the light distribution. Automated bulge-dominated galaxies have a high bulge fraction, are smooth, and have high axis ratios (> 0.65 , i.e., are roundish); automated disc-dominated galaxies either have low bulge fraction or are lumpy or are elongated (axis ratio ≤ 0.45); and automated intermediates are all other cases. Measuring the success of the automated classifications as given by the reliability and completeness of the sub-samples, both the automated bulge and disc samples have reliability $\sim 70\%$ and completenesses of 75% and 83%, respectively.

Therefore while axis ratio alone is not a good parameter to separate ETGs from LTGs, we attempt to use it as an additional parameter to improve the separation based on concentration index. From §3.1 we choose the concentration index 2.6 since it gives very high ETG completeness (see [Table 1](#)) and make additional axis ratio cuts to improve the reliability. In [Figure 24](#) and [Table 2](#) we show the axis ratio-concentration index plane and the result of cuts in the two parameters, respectively.

[Table 2](#) shows that cuts at subsequently higher axis ratios result in a marginal improvement to the ETG reliability. The highest improvement yields 65% using $C \geq 2.6$ and $b/a \geq 0.6$, but at that point almost half of the ETGs are lost. This cut combination is similar to increasingly larger concentration-only cuts as can be compared from [Table 1](#). Again the situation for the LTGs is better, since an axis ratio cut at $b/a < 0.6$ yields a completeness 23% higher with only a 12% reduction in reliability compared to concentration index cuts.

In the next section we add a third parameter used in automated galaxy classification to the concentration index and axis ratio cuts described above.

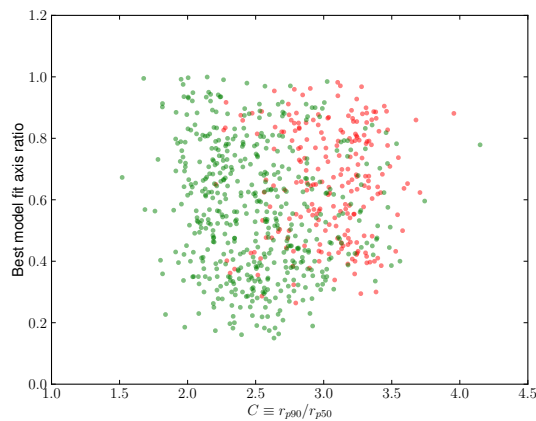


Figure 24: Best fit axis ratio as a function of concentration index for ETGs (red circles) and LTGs (green circles).

ETGs	rel (%)	comp (%)	LTGs	rel (%)	comp (%)
$C \geq 2.6$	52	91	$C < 2.6$	94	64
and $b/a \geq 0.3$	54	90	or $b/a < 0.3$	94	67
“ 0.4	58	84	“ 0.4	91	73
“ 0.5	61	68	“ 0.5	85	81
“ 0.6	65	56	“ 0.6	82	87
and $P_{\text{deV}} > P_{\text{exp}}$	60	86	or $P_{\text{deV}} < P_{\text{exp}}$	93	75
“	63	82	“	91	79
“	65	67	“	85	84
“	66	54	“	81	88

Table 2: Reliability (rel) and completeness (comp) achieved when combining cuts in photometric parameters.

3.4 PROFILE TYPE

As was mentioned in §3.3, the SDSS pipeline outputs the χ^2 likelihoods of the model fits to the light distribution of the galaxies. For all of the galaxies one of the profile type, either P_{deV} or P_{exp} , was much larger than the other, so it is easy to decide whether a galaxy is better represented by a de Vaucouleurs or exponential profile. We assign to each galaxy a light profile flag, either *deV* or *exp*, depending on which light profile is deemed more likely by the SDSS pipeline. We show the distribution of profile types for ETGs and LTGs as a function of magnitude in Figure 25 and Figure 26, respectively, where the galaxies are divided into Petrosian *r*-band absolute magnitude bins. As can be seen in the ETGs the de Vaucouleurs fit dominates at all magnitudes. In the histograms of the LTGs we see the expected transition from brighter, bulge-dominated galaxies better fitted by de Vaucouleurs profiles to dimmer, disc-dominated galaxies better fitted with exponential profiles.

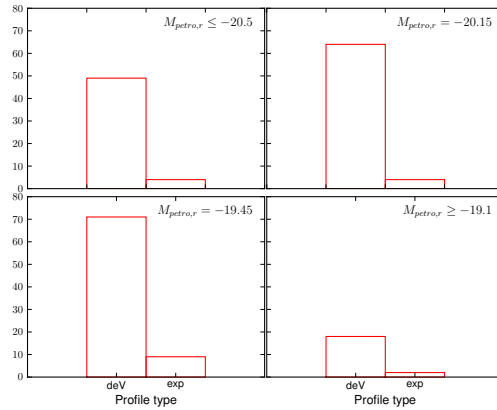


Figure 25: Histogram of profile type for the ETGs in Petrosian *r*-band absolute magnitude bins $M_{\text{petro},r} \leq -20.5$ (top left), $-20.5 \leq M_{\text{petro},r} \leq -19.8$ (top right), $-19.8 \leq M_{\text{petro},r} \leq -19.1$ (bottom left) and $M_{\text{petro},r} \geq -19.1$ (bottom right).

From these histograms it is evident that the use of only profile likelihoods for automated galaxy classification has limited usefulness at high magnitudes. Figure 27 shows the axis ratio-concentration index plane with circle markers for $P_{\text{deV}} > P_{\text{exp}}$

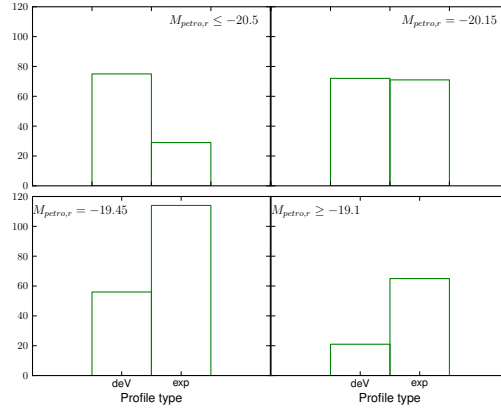


Figure 26: Histogram of profile type for the LTGs in Petrosian r -band absolute magnitude bins $M_{\text{petro},r} \leq -20.5$ (top left), $-20.5 \leq M_{\text{petro},r} \leq -19.8$ (top right), $-19.8 \leq M_{\text{petro},r} \leq -19.1$ (bottom left) and $M_{\text{petro},r} \geq -19.1$ (bottom right).

and square markers for $P_{\text{exp}} > P_{\text{deV}}$. The majority of LTGs with exponential profiles have small axis ratios and low concentration indices, and in this region there is low contamination from other types. Meanwhile de Vaucouleurs LTGs are scattered over the plane. Out of the 221 ETGs in our sample, 202 are fitted by de Vaucouleurs profiles and 19 are fitted by exponential profiles in the SDSS.

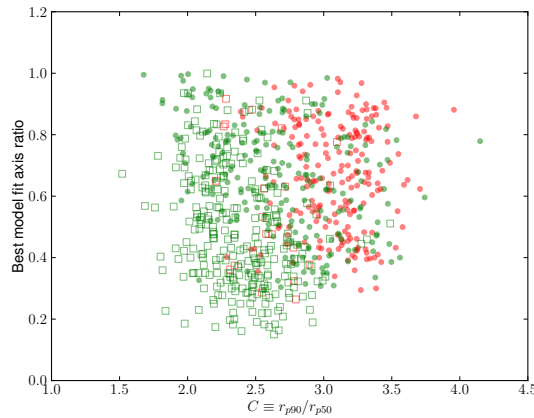


Figure 27: Best fit axis ratio a/b as a function of concentration index for ETGs (red colors) and LTGs (green colors) with $P_{\text{deV}} > P_{\text{exp}}$ (circles) or $P_{\text{exp}} > P_{\text{deV}}$ (squares).

[Table 2](#) shows the reliability and completeness achieved when the profile type is combined with our choice of concentration index and axis ratio cuts in the ETGs, and the reliability and completeness of profile type cuts in the LTGs. The completeness of the ETGs is reduced by small amounts while the reliability increases relative to previous cuts. For the LTGs, profile type cuts yield slightly worse reliability, while they increase the completeness. However adding profile type cuts to concentration index and axis ratio cuts is similar to higher concentration-only cuts, as can be seen by comparing with the values in [Table 1](#).

To summarize, we have shown that our attempts to improve the concentration-based separation of ETGs and LTGs using additional SDSS parameters are only marginally successful. In particular, starting from a concentration cut at $C = 2.6$ and adding selection criteria based on axis ratio and profile type yields a similar completeness and reliability as using a concentration-only cut at the higher $C = 2.9$.

In this section we have used SDSS profile analysis, which is limited to the two extreme cases of de Vaucouleurs and exponential profiles. But as was mentioned in §1.2 galaxy profiles can be fitted using Equation 2, the general profile shape from which the other two are just special cases. Next we explore whether light profiles are useful when parameterised in this way.

3.5 SÉRSIC INDEX

The NYU-VAGC catalog provides one-component Sérsic fits for a large number of galaxies in the SDSS (Blanton et al. 2005b). We extract the Sérsic index n from this catalog. In Figure 28 we show the distribution of n , while in Figure 29 the galaxies are separated into different Petrosian r -band absolute magnitude bins. Here we can see the transition from faint, disk-dominated spirals (small $n \sim 1$) to bright, bulge-dominated Sa's (larger $n \sim 4$).

It is immediately evident that automated galaxy classifications based only on Sérsic index will result in ETG samples with a severe contamination of LTGs and vice versa. Figure 30 shows the expected correlation between n and concentration index.

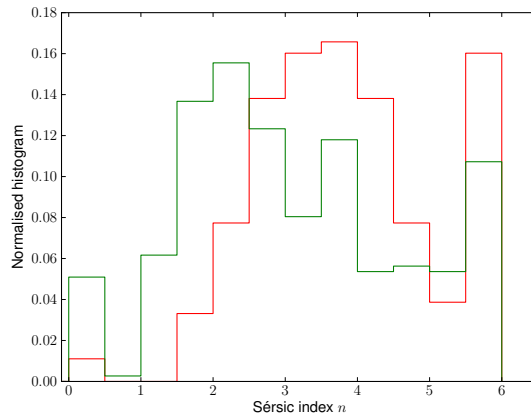


Figure 28: Normalized histogram of Sérsic index for ETGs (green lines) and LTGs (red lines), where each distribution has been normalized by the total number of galaxies in the respective sub-sample.

3.6 SUMMARY

We have seen the complicated interplay between reliability and completeness, for both ETG and LTG sub-samples defined on the basis of SDSS parameters. Starting with the concentration index, many LTGs have indices as high as those of most ETGs. Addi-

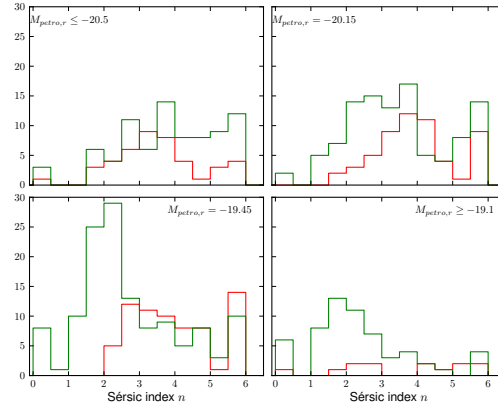


Figure 29: Histogram of Sérsic index for ETGs (green lines) and LTGs (red lines) separated in Petrosian r -band absolute magnitude bins $M_{\text{petro},r} \leq -20.5$ (top left), $-20.5 \leq M_{\text{petro},r} \leq -19.8$ (top right), $-19.8 \leq M_{\text{petro},r} \leq -19.1$ (bottom left) and $M_{\text{petro},r} \geq -19.1$ (bottom right).

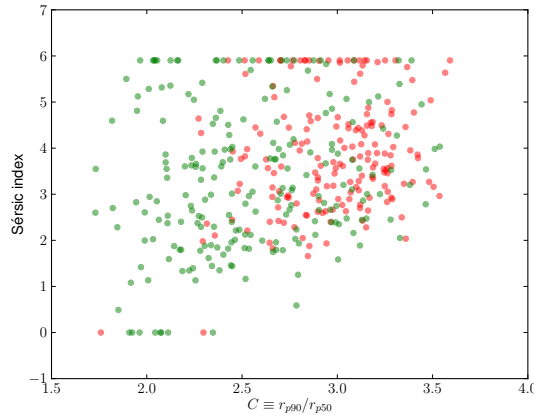


Figure 30: Sérsic index as a function of concentration index for ETGs (red circles) and LTGs (green circles). The LTG NGC5746 is excluded from the plot since it has an outlying NYU-VAGC concentration index of 4.9.

tional cuts in photometric parameters are only marginally successful in refining the overlap.

Overall, the result of combining various parameters (e. g., concentration index, axis ratio and light profile type) results in a similar completeness and reliability as simply using a different cut in one single parameter, concentration. Also, we have shown that mean surface brightness, another parameter often used in the literature, is basically equivalent to concentration as far as sample selection is concerned.

The main reason why global photometric parameters are unable to separate ETGs from LTGs is that these galaxies are structurally very similar, as is starting to be recognized widely (van den Bergh 1976; Cappellari et al. 2011b; Kormendy & Bender 2012), and the real difference between these two types are local properties (dust, spiral arms, clumpiness) which are lost in the global parameters.

For example, analysis of the ATLAS^{3D} ETGs has shown that there is a continuity in the stellar kinematics of the flattest ellipticals and the S0's with the largest bulges (Cappellari et al. 2011b). Furthermore, if these ETGs are nearly edge-on the structure seen in optical images is extremely similar to that of edge-on LTGs, with the exception that the latter have prominent dust lanes. For instance, in Figure 18 compare the two galaxies at row 5, columns 3 and 4. The cold gas properties are the main difference between ETGs and LTGs (Serra et al. 2012).

In the following chapter we adopt two simple cuts, one in concentration at $C = 2.9$ and one in mean surface brightness at $\langle \mu_{r_{p50}} \rangle = 19.5 \text{ mag/arcsec}^2$. We then study the ETGs and LTGS above and below the cuts, and analyze how such a definition affects the conclusion of HI studies of galaxies of different type.

H I PROPERTIES

As was discussed (§3), galaxy concentration is the best and concurrently simplest quantification of galaxy morphology. Also surface brightness is highly correlated to galaxy concentration (§3.2) and morphology. In turn a galaxy’s morphology is a proxy for its recent history, in terms of mergers and star formation. Analysis of how the H I mass and H I mass-to-luminosity ratio correlate with photometric parameters that themselves correlate with morphology therefore probes the relation between galaxy formation and evolution and cold H I gas.

In this chapter we analyze the H I mass $M(\text{H I})$ [M_{\odot}] and H I mass-to-luminosity ratio $M(\text{H I})/L_{\text{K}}$ [M_{\odot}/L_{\odot}] as a function of concentration index and mean surface brightness. From [Serra et al. \(2012\)](#) we obtain H I mass for 48 detected ETGs and upper limits for 98 undetected ETGs out of the 221 ETGs, and for 314 out of the 503 LTGs matched in §2. Five ETGs detected in H I by [Serra et al. \(2012\)](#) we do not have an SDSS match for (§2) and therefore are not included in the following analysis¹. Luminosities are calculated using:

$$L_{\text{K}} = 10^{-0.4(M_{\text{K}} - M_{\odot, \text{K}})} \quad (11)$$

where M_{K} is given in Tables 3 and 4 of [Cappellari et al. \(2011a\)](#) and $M_{\odot, \text{K}} = 3.28$ mag.

Histograms of $M(\text{H I})$ and $M(\text{H I})/L_{\text{K}}$ are shown in [Figure 31](#) and [Figure 32](#), respectively, where the distributions have been normalized by the total number of galaxies in the respective ETG and LTG sub-sample. The ETGs included in this sample span the range of low-H I mass to high-H I mass and H I mass-to-luminosity ratio found in [Serra et al. \(2012\)](#), and the LTGs show the peak at high H I mass and high H I mass-to-luminosity ratio with a tail at low values of both H I quantities.

Each of the ETGs detected in the ATLAS^{3D} H I sample is designated into one of four classes according to the following H I kinematics and morphology:

- *D (large discs)*: Regular kinematics and morphology of a disc or ring with radius $R(\text{H I}) > 3.5 \times R_e$.
- *d (small discs)*: Regular kinematics and morphology of a disc with radius $R(\text{H I}) < 3.5 \times R_e$.
- *u (unsettled)*: Irregular kinematics and unsettled morphology, e.g., tails or streams.
- *c (clouds)*: H I distributed in small, scattered clouds.

where the radius $R(\text{H I})$ is defined as the maximum distance of the $N(\text{H I}) = 5 \times 10^{19} \text{ cm}^{-2}$ isophote from the galaxy center and R_e is the projected half-light effective radius

¹ The missing ETGs are: NGC1023, NGC2768, NGC3608, NGC4406, and NGC6798.

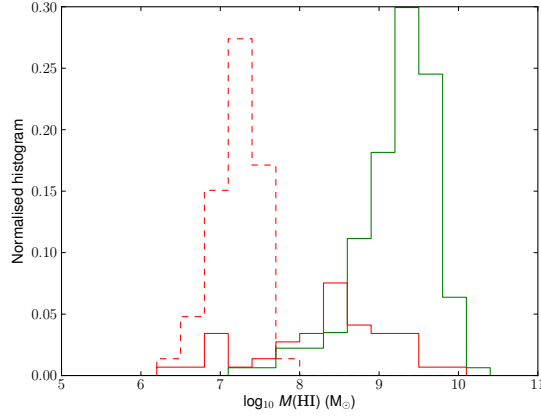


Figure 31: Normalised $M(\text{HI})$ distribution of detected ETGs (red lines), undetected ETGs (dashed red lines), and LTGs (green lines) included from the ATLAS^{3D} HI sample. Masses were obtained from Table B1 in [Serra et al. \(2012\)](#).

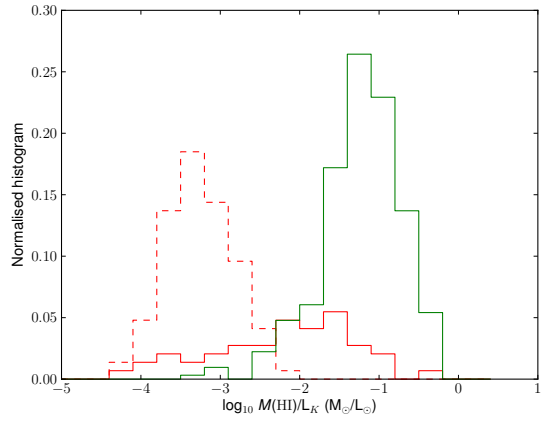


Figure 32: Normalised $M(\text{HI})/L_K$ distribution of detected ETGs (red lines), undetected ETGs (dashed red lines, upper limits), and LTGs (green lines) included from the ATLAS^{3D} HI sample.

in arcsec. HI morphology comes from visual inspection of total-HI maps in relation to optical images. In our sample we have 23 out of the 24 D's, all 10 d's, 4 out of 5 c's, and 11 out of 14 u's. We also include these HI morphologies and analyze how they relate to galaxy concentration and mean surface brightness.

4.1 HI MASS

[Figure 33](#) shows $M(\text{HI})$ as a function of concentration index, with different red symbols representing HI morphology as indicated in the legend. The horizontal dotted line is at $M(\text{HI}) = 5 \times 10^8 M_\odot$ below which 129/146=88% of the ETGs lie and above which 270/314=86% of the LTGs lie, which is comparable to the values in [Serra et al. \(2012\)](#). This plot (and other, similar plots in this chapter) show that HI mass is a much better way of separating ETGs from LTGs than any SDSS parameter.

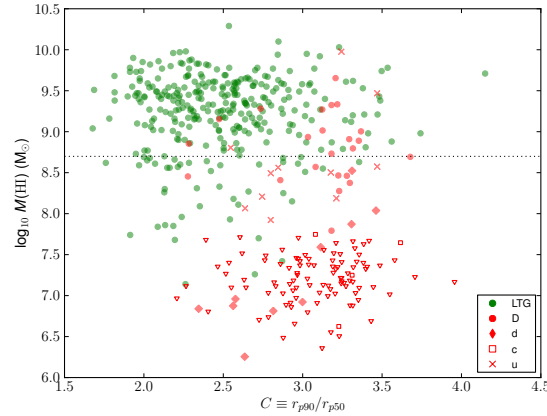


Figure 33: $M(\text{HI})$ as a function of concentration index for undetected ETGs (red upside-down triangles), LTGs (green circles), and detected ETGs with different symbols representing H I morphology as indicated in the legend. The horizontal dotted line is at $M(\text{HI}) = 5 \times 10^8 M_{\odot}$.

All ETGs close to the HI mass where the galaxy ratio transitions from majority-LTG to majority-ETG, have unsettled or large disc HI morphologies. The only exception is 1 high-concentration d. The high $M(\text{HI})$ -low concentration quadrant is dominated by LTGs. Three ETGs with large HI discs (D's) are still in this region and are exceptional cases, since the large majority of D's have much higher concentration indices (18/23 = 78% have $C \geq 3.0$). The number of LTGs trickles down at subsequently lower $M(\text{HI})$ and is confined to lower concentration indices.

A similar scenario appears in the $M(\text{HI})$ -mean surface brightness plane shown in Figure 34.

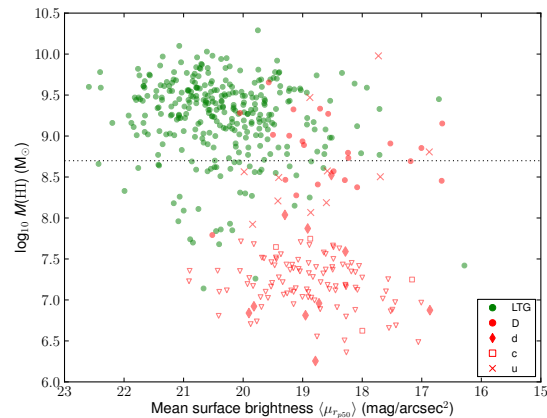


Figure 34: $M(\text{HI})$ as a function of surface brightness for undetected ETGs (red upside-down triangles), LTGs (green circles), and detected ETGs with different symbols representing H I morphology as indicated in the legend. The horizontal dotted line is at $M(\text{HI}) = 5 \times 10^8 M_{\odot}$.

4.2 HI MASS-TO-LUMINOSITY RATIO

Catinella et al. (2010) study scaling relations between HI quantities and photometric parameters of $\sim 1,000$ galaxies. These have available optical spectroscopy from the SDSS, ultraviolet imaging from the Galaxy Evolution Explorer (GALEX, Martin et al. 2005), and many are covered by ALFALFA or found in the Cornell HI digital archive. The authors find that the HI mass fraction, defined as the ratio of HI-to-stellar mass $M(\text{HI})/M_*$, correlates better with stellar mass surface density (defined as $\mu_* = 0.5M_*/\pi(r_{50,z})^2 M_\odot \text{ kpc}^{-2}$) than with concentration index.

The $M(\text{HI})/L_K$ as a function of concentration index and mean surface brightness is shown in Figure 35 and Figure 36. The horizontal dotted line in each of the panels marks $M(\text{HI})/L_K = 10^{-2.5} M_\odot/L_\odot$ below which 113/146=77% of the ETGs lie and above which 307/314=98% of the LTGs lie, which is comparable to values in Serra et al. (2012). The vertical dashed line in Figure 35 is at $C = 2.9$ and the vertical dashed line in Figure 36 is at $\langle \mu_{r_{p50}} \rangle = 19.5 \text{ mag/arcsec}^2$, which are the most sensible values that can be adopted following the discussion in §3.

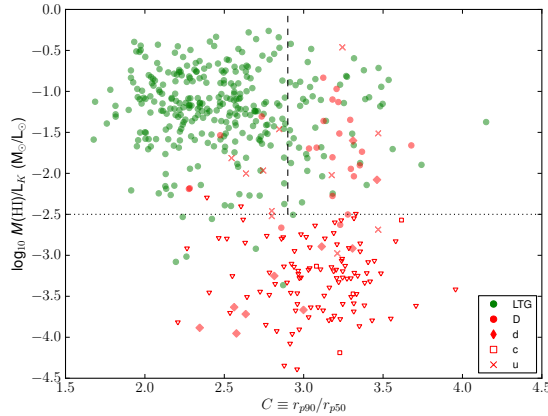


Figure 35: $M(\text{HI})/L_K$ against concentration index for undetected ETGs (red upside-down triangles), LTGs (green circles), and detected ETGs with different symbols representing HI morphology as indicated in the legend.

Inspection of the figures shows some important points. We find larger scatter for $M(\text{HI})/L_K$ against concentration index as compared to against mean surface brightness. Moving towards lower ratios and higher mean surface brightnesses, ETGs start to appear and the LTGs start to scatter further. At the smallest $M(\text{HI})/L_K$ and highest mean surface brightnesses we find no LTGs, with the exception of 1 outlier. Here is where all of the undetected ETGs are found.

Focusing on mean surface brightness, there are 3 regions each with a substantially different galaxy mix. The region $M(\text{HI})/L_K \geq -2.5 M_\odot/L_\odot$ and $\langle \mu_{r_{p50}} \rangle \geq 19.5 \text{ mag/arcsec}^2$ is dominated by LTGs with a ratio 261/267=98% there; this is 261/314=83% of the LTG total. All of the region below $M(\text{HI})/L_K < -2.5 M_\odot/L_\odot$ is dominated by ETGs with a ratio 113/120=94% there; this is 113/146=77% of the ETG total. In the quadrant demarcated by $M(\text{HI})/L_K \geq -2.5 M_\odot/L_\odot$ and $\langle \mu_{r_{p50}} \rangle \leq 19.5 \text{ mag/arcsec}^2$ the galaxy ‘population’ is a mixture of LTGs and ETGs with large HI discs, with some

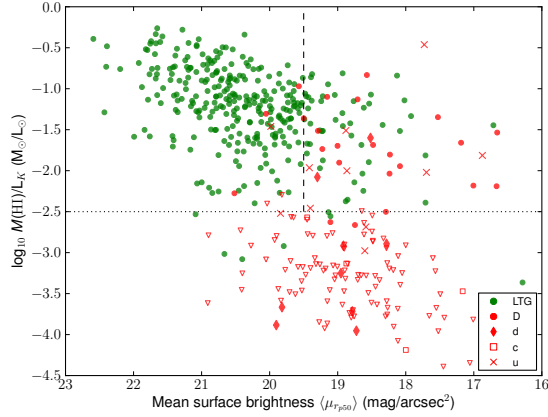


Figure 36: $M(\text{HI})/L_K$ against mean surface brightness for undetected ETGs (red upside-down triangles), LTGs (green circles), and detected ETGs with different symbols representing HI morphology as indicated in the legend.

HI unsettled ETGs and 2 small HI discs. In total there are 27 ETGs and 46 LTGs in the quadrant making up 37% and 63%, respectively, of the galaxies there.

We plot a color-magnitude diagram highlighting the 73 galaxies with $M(\text{HI})/L_K \geq -2.5 M_\odot/L_\odot$ and $\langle \mu_{r,50} \rangle \leq 19.5 \text{ mag/arcsec}^2$ in Figure 37. Most of the 27 ETGs stay within the tight ETG color-magnitude relation, while the 46 LTGs overlap with the ETGs and scatter around the diagram. It might be useful to instead use a color which discriminates better between young and old stars (e. g., $NUV-r$). Figure 38 shows the T -type distribution of these 73 galaxies (shaded histograms) and overlapped the same histogram for all the galaxies in our sample. The 27 ETGs span the same T -type range as all the ETGs, while the 46 LTGs have earlier T -types than all the LTGs.

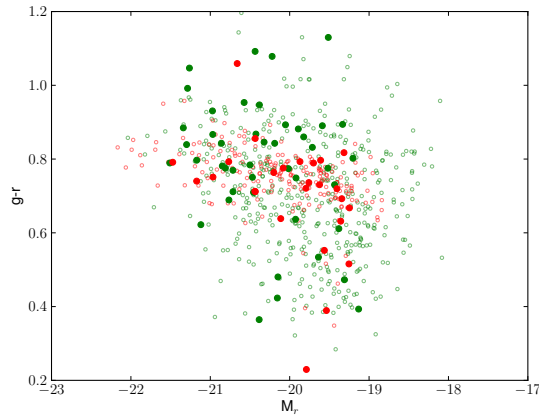


Figure 37: Galactic extinction-corrected color-magnitude diagram for ETGs (large red circles) and LTGs (large green circles) with $M(\text{HI})/L_K \geq -2.5 M_\odot/L_\odot$ and $\langle \mu_{r,50} \rangle \leq 19.5 \text{ mag/arcsec}^2$, and for all other ETGs (red rings) and LTGs (green rings).

SDSS images of the 27 ETGs are shown in Figure 39 and of the 46 LTGs in Figure 40. The ETGs have very similar visual appearance while many of the LTGs appear fea-

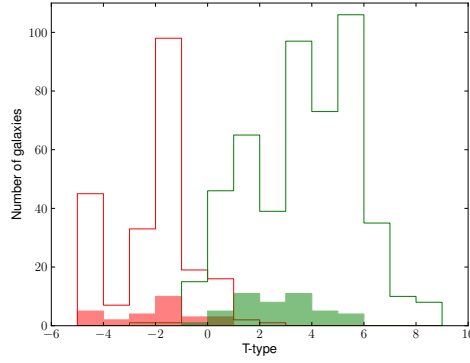


Figure 38: Histogram of T -type for ETGs (shaded red) and LTGs (shaded green) with $M(\text{H I})/L_K \geq -2.5 M_\odot/L_\odot$ and $\langle \mu_{r,p50} \rangle \leq 19.5 \text{ mag/arcsec}^2$, and for all other ETGs (red lines) and LTGs (green lines).

tureless and may be objects intermediate between the ETG and LTG morphology (e. g., NGC4138, NGC4369, NGC7742). However the fine structure morphologies of the two types are quite different and distinguish the two types more precisely. These galaxies have been classified as having different morphology, but have similar H I, concentration, and mean surface brightness, while also atypical properties when compared to galaxies of the same type.



Figure 39: The 27 ETGs with $M(\text{H I})/L_K \geq -2.5 M_\odot/L_\odot$ and $\langle \mu_{r,p50} \rangle \leq 19.5 \text{ mag/arcsec}^2$. The top row of each image gives the galaxy name and the code for the H I morphology where D = large disc, d = small disc, and u = unsettled. There is one undetected ETG (row 5, column 4) and no c's.

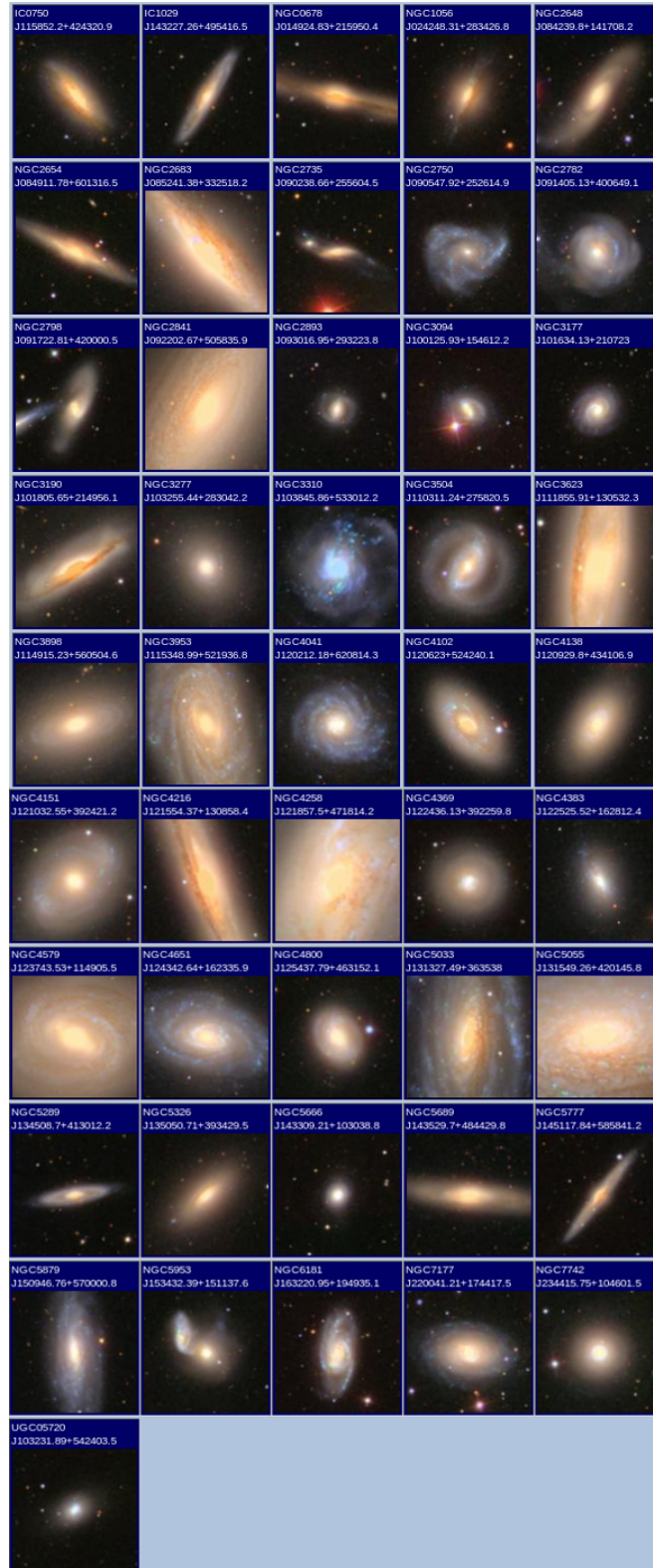


Figure 40: The 46 LTGs with $M(\text{HI})/L_K \geq -2.5 M_\odot/L_\odot$ and $\langle \mu_{\text{rp},50} \rangle \leq 19.5$ mag/arcsec².

4.3 HI PROPERTIES OF GALAXIES CLASSIFIED BY AUTOMATED METHODS

As was discussed in §3 the concentration index and mean surface brightness are photometric parameters commonly used to define samples of early and late-type galaxies. We analyze how concentration index and mean surface brightness cuts affect the HI properties of the resulting sub-samples.

We first apply a classification in which the concentration index of 2.9 is used to separate galaxies. All galaxies with $C \geq 2.9$ or $C < 2.9$ are grouped. The first cut corresponds to that commonly used for selecting ETGs while the latter to that used for LTGs. We compare the HI properties of the two sub-samples $M(\text{HI})$ and $M(\text{HI})/L_K$ in Figure 41 and Figure 42, respectively. These should be compared with Figure 31 and Figure 32.

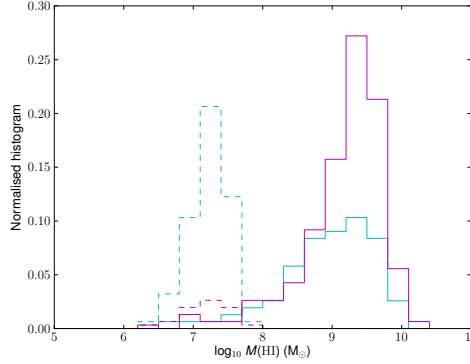


Figure 41: Distribution of $M(\text{HI})$ for galaxies classified using $C \geq 2.9$ (light blue lines) or $C < 2.9$ (pink lines), with dashed lines for undetected ETGs.

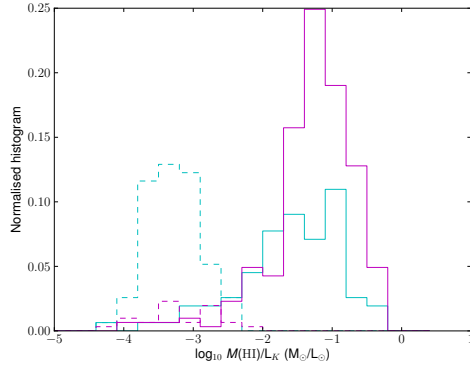


Figure 42: Distribution of $M(\text{HI})/L_K$ for galaxies classified using $C \geq 2.9$ (light blue lines) or $C < 2.9$ (pink lines), with dashed lines for undetected ETGs.

The second cut we study is at a mean surface brightness of $19.5 \text{ mag/arcsec}^2$. All galaxies with $\langle \mu_{r_{p50}} \rangle < 19.5 \text{ mag/arcsec}^2$ or $\langle \mu_{r_{p50}} \rangle \geq 19.5 \text{ mag/arcsec}^2$ are grouped. The first cut corresponds to values expected for ETGs while the latter to values expected for LTGs. Distributions of $M(\text{HI})$ and $M(\text{HI})/L_K$ of these sub-samples are

shown in Figure 43 and Figure 44, respectively. These should be compared with Figure 31 and Figure 32.

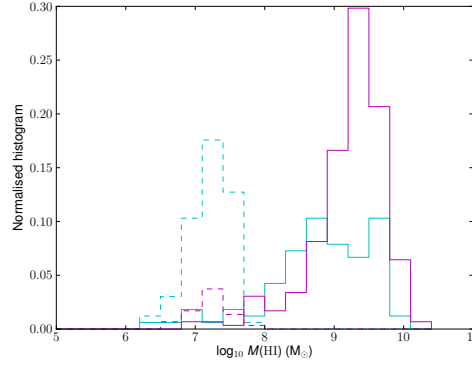


Figure 43: Distribution of $M(\text{HI})$ for galaxies classified using $\langle \mu_{r_{p50}} \rangle < 19.5$ mag/arcsec² (light blue lines) and $\langle \mu_{r_{p50}} \rangle \geq 19.5$ mag/arcsec² (pink lines), with dashed lines for undetected ETGs.

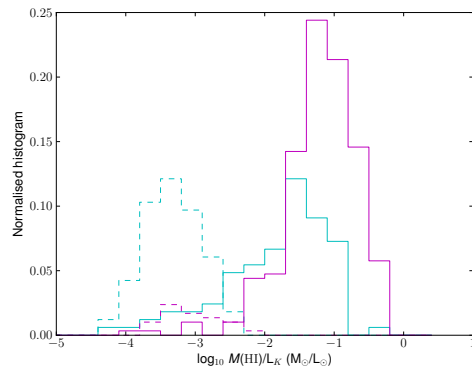


Figure 44: Distribution of $M(\text{HI})/L_K$ for galaxies classified using $\langle \mu_{r_{p50}} \rangle < 19.5$ mag/arcsec² (light blue lines) and $\langle \mu_{r_{p50}} \rangle \geq 19.5$ mag/arcsec² (pink lines), with dashed lines for undetected ETGs.

These figures show that galaxies with high concentration (or mean surface brightness), which is expected for ETGs, exhibit a peak at high $M(\text{HI})$ and $M(\text{HI})/L_K$. This is in strong contrast with the $M(\text{HI})$ and $M(\text{HI})/L_K$ histograms of visually classified ETGs, where the HI-rich ETGs cover broad distributions. Therefore selecting galaxies using concentration index or mean surface brightness cuts will give HI distributions which do not correspond with those derived from visually classified galaxies. This is due to the overlap in the photometric properties of ETGs and LTGs, and the selection of a mix of galaxy types using such parameters.

SUMMARY

We have analyzed how galaxy automated classification maps onto visual classification. Equivalent reliability and completeness can be achieved in sub-samples selected through single cuts in concentration index, or the similar mean surface brightness, and sub-samples selected through photometric parameter combinations. Global photometry of ETGs and LTGs misses the fine-structure morphology that distinguishes the two types, such as spiral arms, and thus provides only crude classification.

The $M(\text{H}\text{I})/L_K$ as a function of concentration index and mean surface brightness plots show there are 3 regions each with a substantially different galaxy mix. In the quadrant demarcated by $M(\text{H}\text{I})/L_K \geq -2.5 M_\odot/L_\odot$ and $\langle \mu_{r,p50} \rangle \leq 19.5 \text{ mag/arcsec}^2$ there are 37% ETGs and 63% LTGs. These galaxies have been classified as having different morphology, but have similar H I and mean surface brightness (and concentration), while also atypical properties when compared to galaxies of the same type which lie in the other 2 regions.

The H I properties of ETG and LTG sub-samples classified using automated or visual methods are substantially different. Automated methods employing concentration index and mean surface brightness to select early-type sub-samples include more high- $M(\text{H}\text{I})$ and $M(\text{H}\text{I})/L_K$ galaxies, seen as a peak in these distributions, and contrasts with the distributions derived from visually selected early-type sub-samples.

The main conclusions stated throughout the thesis are:

- §3.1: The reliability of an ETG selection based on C is never better than 72%, due to the fact that a large fraction of LTGs have concentrations as high as that of most ETGs.
- §3.1: Though there is high overlap in ETGs and LTGs at intermediate concentration indices, visual inspection of images shows fine structure morphology that differs between the two types. Quantifying this fine structure is therefore the only way we see to improve the agreement between visual classification and classification based on global SDSS parameters (e. g., CAS system in [Conselice 2003](#)).
- §3.1: The reliability and completeness achieved using concentration index cuts is consistent between relatively large (e. g., [Nair & Abraham 2010](#)) and small galaxy samples (e. g., [Cappellari et al. 2011a](#)).
- §3.2: Mean surface brightness correlates well with concentration index, and this translates into similar reliability and completeness in sub-samples classified with either photometric measure (surface brightness may be just slightly better).

- §3: Adding photometric parameter cuts in axis ratio and profile type has the same result as increasing the value of a concentration index only cut.
- §3.5: Classification of galaxies using parameters derived from flexible fits such as the Sérsic model is likely to be worse than classification of galaxies using concentration index cuts.
- §4.1-§4.2: In the $M(\text{H I})/L_K$ vs. mean surface brightness plot we find regions populated by ETGs or LTGs only. The only overlap region is one of galaxies with high mean surface brightness (or C) and high $M(\text{H I})/L_K$. From these plots it appears that H I (and not C or $\langle\mu_{r_{p50}}\rangle$) is an excellent observable to separate ETGs from LTGs.
- §4.3: Classifying galaxies using C and $\langle\mu_{r_{p50}}\rangle$ yields $M(\text{H I})$ and $M(\text{H I})/L_K$ distributions that do not match the corresponding distributions derived from visually classified galaxies. In particular, samples of ETGs defined using C or $\langle\mu_{r_{p50}}\rangle$ have a much larger population of H I rich galaxies compared to samples of ETGs defined on the basis of visual morphology.

6

APPENDIX OF TABLES

6.1 GALAXIES SELECTED FROM MULTIPLE MATCHES

Galaxy	Type	ObjectID	Distance (arcsec)	r_{p90} (arcsec)	modelMag_r (mag)
(1)	(2)	(3)	(4)	(5)	(6)
NGC5866	ETG	127671766924263460	3.893	54.732	10.176
PGC016060	ETG	127676305095262242	0.595	19.875	13.39
IC1048	LTG	127654881276395557	2.619	36.148	12.912
NGC3227	LTG	127667735033807039	0.765	60.91	12.274
NGC3424	LTG	127665016311644292	1.593	22.295	12.61
NGC3705	LTG	127660613437947914	1.0	37.242	12.031
NGC3976	LTG	127661970646040621	7.83	20.414	12.01
NGC4194	LTG	127658916918984717	5.479	26.062	13.035
NGC4402	LTG	127658630768885823	40.613	47.149	12.235
NGC4536	LTG	127651753477210142	1.809	82.67	11.643
NGC4586	LTG	127655124474593475	0.502	63.478	11.943
NGC5363	LTG	127654881271283774	1.427	56.806	10.212
NGC5372	LTG	127659146704846884	1.719	14.591	13.24
NGC5523	LTG	127665532785459210	1.243	55.52	12.869
NGC5690	LTG	127651736847974422	13.108	64.659	12.908
NGC5981	LTG	127671939262447835	12.481	52.887	13.139
NGC7241	LTG	127680297807314978	10.66	56.262	12.597
UGC00260	LTG	127678857937617063	1.453	55.12	13.487
UGC04306	LTG	127674290221023256	0.903	25.792	13.585
UGC06023	LTG	127667252933754936	11.221	32.824	12.98

List and parameters of galaxies selected. *Note.* Column (2): Obtained from [Cappellari et al. \(2011a\)](#). Columns (3), (5), and (6): Obtained from SDSS. Column (4): Calculated using [Equation 4](#).

6.2 GALAXIES WITH DISTANCE > 5 ARCSEC

Galaxy	Type	ObjectID	Distance (arcsec)	$r_{p,90}$ (arcsec)	modelMag_r (mag)	Decision
(1)	(2)	(3)	(4)	(5)	(6)	(7)
IC1024	ETG	1237651821099614262	5.216	22.791	13.108	I
NGC4636	ETG	1237651736835391570	53.101	80.168	12.412	E
NGC0520	LTG	1237678621699735568	10.74	77.187	11.837	I
NGC2770	LTG	1237664869211504780	13.989	56.974	12.15	E
NGC2785	LTG	1237658206107664445	8.159	39.859	13.149	E
NGC3003	LTG	1237664668432138249	6.95	39.716	12.41	I
NGC3198	LTG	1237658612513374224	12.048	72.456	11.203	I
NGC3627	LTG	1237661813879144461	57.507	70.104	12.762	E
NGC3628	LTG	1237664130485059614	11.79	75.951	10.662	I
NGC4010	LTG	1237660635465711701	8.408	76.529	12.692	I
NGC4205	LTG	1237654608531095641	22.588	27.734	13.31	E
NGC4217	LTG	1237661357007241235	5.975	90.818	11.214	I
NGC4389	LTG	1237661852006744092	7.679	47.895	11.827	I
NGC4414	LTG	1237665328779231262	33.914	56.542	11.351	E
NGC4437	LTG	1237648704579174432	18.886	116.517	11.74	I
NGC4532	LTG	1237661974401253489	9.804	44.706	12.23	I
NGC4631	LTG	1237665330391285816	34.563	82.118	11.812	E
NGC5496	LTG	1237648702979375194	7.814	68.609	13.274	I
NGC5907	LTG	1237651250435129428	10.24	88.765	10.992	I
UGC03053	LTG	1237664088606572620	22.817	73.199	13.808	E
UGC05459	LTG	1237657771247403132	5.374	64.329	12.874	E
UGC12010	LTG	1237669696762347622	5.696	28.216	14.354	E

List and parameters of galaxies selected. *Note.* Column (2): Obtained from [Cappellari et al. \(2011a\)](#). Columns (3), (5), and (6): Obtained from SDSS. Column (4): Calculated using [Equation 4](#). Column (7): Included galaxies are labeled with *I*, while excluded galaxies are labeled with *E*.

6.3 MAGNITUDE-VS-RADIUS OUTLIERS

Galaxy	ObjectID	Distance (arcsec)	r_{p90} (arcsec)	modelMag_r (mag)
(1)	(2)	(3)	(4)	(5)
NGC0573	1237666214081855505	0.426	1.724	16.705
NGC0660	1237653651309002968	1.832	1.424	16.687
NGC3395	1237665128535752751	0.476	1.495	16.852
NGC3556	1237657611263213608	1.54	1.938	16.554
NGC4298	1237661069263372370	0.581	2.02	16.631
NGC4567	1237661815485104152	0.338	2.203	15.34
NGC4691	1237671264958349432	0.299	1.421	16.066
NGC5970	1237668270838579404	0.701	1.393	16.6

List and parameters of outliers in [Figure 4](#). *Note.* Columns (3), (5), and (6): Obtained from SDSS. Column (4): Calculated using [Equation 4](#).

BIBLIOGRAPHY

- K. Abazajian et al. *ApJS*, 182:543, 2009.
- M. Balogh et al. *MNRAS*, 348:1355, 2004.
- D. Barnes et al. *MNRAS*, 322:486, 2001.
- E. Bell et al. *ApJS*, 149:289, 2003.
- M. Bernardi et al. *MNRAS*, 404:2087, 2010.
- M. Blanton et al. *AJ*, 121:2358, 2001.
- M. Blanton et al. *AJ*, 129:2562, 2005a.
- M. Blanton et al. *ApJ*, 629:143, 2005b.
- M. Cappellari et al. *MNRAS*, 413:813, 2011a.
- M. Cappellari et al. *MNRAS*, 416:1680, 2011b.
- B. Catinella et al. *MNRAS*, 403:683, 2010.
- J. Cheng et al. *MNRAS*, 412:727, 2011.
- Y. Choi et al. *ApJ*, 658:884, 2007.
- A. Chung et al. *AJ*, 138:1741, 2009.
- C. Conselice. *ApJS*, 147:1, 2003.
- G. de Vaucouleurs. *AnAp*, 11:247D, 1948.
- M. Fukugita et al. *AJ*, 134:579, 2007.
- R. Giovanelli et al. *AJ*, 130:2598, 2005.
- P. Gómez et al. *ApJ*, 584:210, 2003.
- T. Heckman et al. *ApJ*, 613:109, 2004.
- E. Hubble. *ApJ*, 64:321H, 1926.
- E. Hubble. *Realm of the Nebulae*. Yale University Press, 1936.
- J. Hyde & M. Bernardi. *MNRAS*, 394:1978, 2009.
- J. Jeans. *Obs*, 43:389, 1920.
- G. Kauffmann et al. *MNRAS*, 341:33, 2003.
- J. Kormendy. *ApJ*, 218:333, 1977.

- J. Kormendy & R. Bender. *ApJS*, 198:2, 2012.
- M. Longair. *Galaxy Formation*. Berlin: Springer, 2008.
- D. Martin et al. *ApJL*, 619:L1, 2005.
- M. Meyer. In *Panoramic Radio Astronomy: Wide-field 1-2 GHz Research on Galaxy Evolution*, 2009.
- M. Meyer et al. *MNRAS*, 350:1195, 2004.
- W. Morgan. *PASP*, 70:364, 1958.
- R. Morganti et al. *MNRAS*, 371:157, 2006.
- P. Nair & R. Abraham. *ApJS*, 186:427, 2010.
- O. Nakamura et al. *AJ*, 125:1682, 2003.
- M. Obrić et al. *MNRAS*, 370:1677, 2006.
- T. Oosterloo et al. In *ISKAF2010 Science Meeting*, 2010a.
- T. Oosterloo et al. *MNRAS*, 409:500, 2010b.
- V. Petrosian. *ApJ*, 209L:1P, 1976.
- P. Serra et al. *MNRAS*, 422:1835, 2012.
- J. Sérsic. *BAAA*, 6:41S, 1963.
- S. Shen et al. *MNRAS*, 343:978, 2003.
- R. Sheth et al. *ApJ*, 594:225, 2003.
- K. Shimasaku et al. *AJ*, 122:1238, 2001.
- M. Skrutskie et al. *AJ*, 131:1163, 2006.
- L. Sparke & J. Gallagher, III. *Galaxies in the Universe - 2nd Edition*. Cambridge University Press, 2006.
- J. Strateva et al. *AJ*, 122:1861, 2001.
- C. Tremonti et al. *ApJ*, 613:898, 2004.
- S. van den Bergh. *ApJ*, 206:883, 1976.
- S. van den Bergh. *Galaxy Morphology and Classification*. Cambridge University Press, 1998.
- J. van der Hulst. In *Seeing Through the Dust: The Detection of HI and the Exploration of the ISM in Galaxies*, volume 276, page 84, 2002.

- M. Verheijen et al. In *The Evolution of Galaxies Through the Neutral Hydrogen Window*, volume 1035, page 265, 2008.
- A. West et al. *AJ*, 139:315, 2010.
- O. Wong et al. *MNRAS*, 371:1855, 2006.
- D. York et al. *AJ*, 120:1579, 2000.

ACKNOWLEDGMENTS

This thesis was a fun and challenging journey for me, however I was not the only one involved. . .

Paolo, many thanks for teaching me so much. I feel very proud of having been your student. Tom, many thanks for your comments.

Clareijn, when I started this journey I didn't know I would be writing this sentence. Thank you for just sending me a message to ask if you can help with cleaning my studio. You have been awesome to me.

Mom, thank you for EVERYTHING. I will be tomorrow at Schiphol to meet you. To my brother and sister in Puerto Rico, and their awesome families, I miss you all and hope to see you soon. Marianne and Bas, thank you for taking me in and being very kind, and for speaking English a lot of the times.

Solimar, thank you for always being there to listen and to talk about plátanos. To the Kapteyners, especially Sofia & Thomas, Oscar V., Bertrand L., Yunhee, Yanping, Keimpe, Johan, Omar, Pratyush, and last but never least Sanaz, thank you for the funny times and memorable experiences. Katinka, thank you for your friendship and for that youtube link about Charlie the unicorn.

Marc, Rien, and Scott, thank you for being such good professors.

And last, the dedication. Not in a section of its own because this is 'just' a master's thesis, but still apart because the contents wouldn't make sense as acknowledgments. I dedicate this thesis to Lucas D. Irisarri (1982-2003) and Lucas M. Irisarri (1945-2008), who by leaving this planet forced me to become stronger. Nine and four years later I can finally put you in a place extremely memorable to me.